NOAA Technical Memorandum OAR PMEL-135

# STANDARDS, CRITERIA, AND PROCEDURES FOR NOAA EVALUATION OF TSUNAMI NUMERICAL MODELS

Costas E. Synolakis[1]
Eddie N. Bernard[2]
Vasily V. Titov[3]
Utku Kânoğlu[4]
Frank I. González[2]


[1] Viterbi School of Civil Engineering
University of Southern California
Los Angeles, CA

[2] Pacific Marine Environmental Laboratory
Seattle, WA

[3] Joint Institute for the Study of the Atmosphere and Ocean (JISAO)
University of Washington, Seattle, WA

[4] Department of Engineering Sciences
Middle East Technical University
Ankara, TURKEY

Pacific Marine Environmental Laboratory
Seattle, WA
May 2007

NOTICE

Mention of a commercial company or product does not constitute an endorsement by NOAA/OAR. Use of information from this publication concerning proprietary products or the tests of such products for publicity or advertising purposes is not authorized.

# Contents

# Standards, criteria, and procedures for NOAA evaluation of tsunami numerical models

C.E. Synolakis[1], E.N. Bernard[2], V.V. Titov[3], U. Kânoğlu[4], F. González[2]

## 1.  Introduction

The National Oceanic and Atmospheric Administration (NOAA) is the federal agency charged with mitigating tsunami hazards in the United States. NOAA's National Weather Service operates the two Tsunami Warning Centers (TWCs) in the U.S., and NOAA has spearheaded the national effort to develop inundation maps for evacuation planning through the National Tsunami Hazard Mitigation Program (NTHMP). The latter was formed through a directive of the U.S. Senate Appropriations Committee in 1994 to develop a plan for a tsunami warning system that reduces the risk to coastal residents. Following the horrific Indian Ocean tsunami of 26 December 2004, the U.S. expanded the role of NTHMP to serve as the organizational framework to implement the recommendations of the National Science and Technology council report "Tsunami Risk Reduction for the United States: A Framework for Action" (NSTC, 2005):

- Develop standardized and coordinated tsunami hazard and risk assessments for all coastal regions of the United States and its territories.

- Improve tsunami and seismic sensor data and infrastructure for better tsunami detection and warning.

- Enhance tsunami forecast and warning capability along our coastlines (Pacific, Atlantic, Caribbean, and Gulf of Mexico) by increasing the number of Deep-ocean Assessment and Reporting of Tsunamis (DART) buoys, tide gauges, and seismic sensors feeding real-time data into on-line forecast models.

- Ensure interoperability between the U.S. national system and other regional tsunami warning systems.

- Provide technical expertise and assistance, as appropriate, to facilitate development of international tsunami and all-hazard warning systems, including for the Indian Ocean.

[1]Viterbi School of Civil Engineering, University of Southern California, Los Angeles, CA 90089-2531, USA

[2]NOAA/Pacific Marine Environmental Laboratory, 7600 Sand Point Way NE, Seattle, WA 98115-6349, USA

[3]Joint Institute for the Study of the Atmosphere and Ocean (JISAO), University of Washington, Box 357941, Seattle, WA 98195-4235, USA

[4]Department of Engineering Sciences, Middle East Technical University, 06531 Ankara, TURKEY

- Encourage data exchange and interoperability among all regional tsunami and all-hazard warning systems, such as the Intergovernmental Oceanographic Sub-commission for the Caribbean (IOCARIBE).

- Promote development of model mitigation measures and encourage communities to adopt construction, critical facilities protection, and land-use planning practices to reduce the impact of future tsunamis.

- Increase outreach to all communities, including all demographics of the at-risk population, to raise awareness, improve preparedness, and encourage the development of tsunami preparedness plans.

- Conduct an annual review of the status of tsunami research and develop a strategic plan for tsunami research in the United States.

Since standards for modeling tools do not currently exist, and given the increased number of states in the Atlantic, the Pacific, and territories in the Caribbean that will need to develop tsunami mitigation plans, there is the risk that forecast products may be produced with older or untested methodology. This is not just a U.S. problem, but worldwide, as UNESCO's plans are to build local capacity for developing maps in most member nations facing tsunami hazards. Incorrectly assessing possible inundation can be costly both in terms of lives lost, or in unnecessary evacuations in areas larger than warranted that may put lives at risk and reduce the credibility of the system, even in areas that were not directly affected. Standards are urgently needed to ensure a minimum level of quality and reliability for forecasting and inundation products.

To calculate tsunami currents, forces and runup on coastal structures, and inundation of coastlines, one must numerically calculate the evolution of the tsunami wave from the deep ocean to its target coastal community. No matter what the numerical model, both validation (the process of ensuring that the model solves the parent equations of motion accurately) and verification (the process of ensuring that the model used represents geophysical reality appropriately) are an essential part of the model development. Validation ensures that the model performs well in a wide range of circumstances and is accomplished through comparison with analytical solutions. Verification ensures that the computational code performs well over a range of geophysical problems. Many existing numerical models have been validated through comparison with analytical solutions. Very few have also been verified with laboratory and field measurements. Even fewer have been tested in an operational forecast setting. Numerical models that have been tested under all three conditions represent the gold standard for both inundation mapping and real-time forecasting.

In the last ten years, the process of model validation and verification has shown that terminal effects of tsunamis can be described by depth-averaged equations. Interest in these equations has arisen because comparisons with both large-scale laboratory data and field data have demonstrated a remarkable and perhaps surprising capability to model complex evolution phenomena, and in particular the maximum runup and inundation, extremely well

over wide ranges of tsunami waves. In the current state of knowledge, the main uncertainty arises from the ambiguities of the initial condition, presuming that the solution methodology solves the equations of motion satisfactorily. With the increasing deployment of tsunameters that monitor the tsunami evolution in the deep ocean and allow for real-time updates of the initial data, this remaining uncertainty is rapidly diminishing.

While equation solvers for more comprehensive approximations of the parent Navier-Stokes equations now exist, they are presently too computationally intensive for inundation mapping or operational forecasting, and are generally used for free-surface flows of very limited geographical extent. These models remain largely unvalidated over wide ranges of tsunami events. Further, the rapid development of packaged numerical modeling tools that allow for the production of high-end animations even by untrained users, underscores the issue of validating specific calculation tools used in tsunami inundation and forecasting to avoid producing mathematically correct, but physically unrealistic solutions.

In this report, benchmark tests for validating and verifying computational tools for predicting the coastal effect of tsunamis are discussed. State-of-the-art methods for validation of tsunami codes are reviewed. Standards and guidelines for validation and verification are recommended for operational codes used for inundation mapping and tsunami forecasting.

## 2.  Model Evaluation Standards

Tsunami inundation models have evolved in the last two decades through careful and explicit validation through comparisons of their predictions with 1+1 (one directional and time) and 2+1 (two directional and time) analytical solutions, laboratory experiments, and field measurements. (See Synolakis and Bernard (2006) for a comprehensive discussion of the evolution of tsunami hydrodynamics.)

Numerical codes often include terms with "friction" factors in an attempt to model physical dissipation, but primarily to stabilize what is an inherently marginal inundation computation, given the small flow depths and large velocities. Large friction factors make calculations more stable, but may under-predict inundation distances and runup heights. Smaller friction factors (or just relying on the inherent numerical dissipation of any numerical calculation) result in more realistic predictions, but they tend to be less stable, depending on the particular differencing scheme used. Thus it is recommended that any code used for modeling tsunami inundation at geophysical scales be tested with all three types of validation data: analytical solutions, laboratory measurements, and field measurements.

While there is in principle no absolute certainty that a numerical code that has performed well in all the benchmark tests will also produce realistic inundation predictions with any given source motions, validated codes largely reduce the level of uncertainty in their results to the uncertainty in the geophysical initial conditions. Further, when coupled with real-time free-field tsunami measurements from tsunameters, validated codes are the only

choice for realistic forecasting of inundation; the consequences of failure are too serious to take chances with less-validated numerical procedures.

In what follows, the steps for validating 2+1 codes are discussed leaving the details of the benchmark problems to Appendix A. Although 1+1 codes were used two decades ago for developing early inundation maps, are generally unreliable for inundation mapping and entirely inadequate for tsunami forecasting. Nonetheless, analytic solutions to the corresponding 1+1 hydrodynamic equations are invaluable to the process of model validation, and several are presented in Appendix A. Specific steps are recommended for the approval of modeling tools, their further development, and their transfer to operations. These steps can be classified into six categories: basic hydrodynamic considerations, analytical benchmarking, laboratory benchmarking, field data benchmarking, scientific evaluations, and operational evaluations.

## 2.1   Basic considerations

Two basic steps are required before benchmarking the numerical codes: mass conservation and convergence.

*Mass conservation*: The first basic step in ensuring that a numerical model accurately simulates tsunami evolution is ensuring that the model conserves mass. While the conservation of mass equation is one of the equations of motion that are solved in any numerical procedure, cumulative numerical approximations can sometimes produce results that violate mass conservation. This is particularly true when friction factors or smoothing to stabilize inundation computations are used. Calculations of conservation of mass should be such that the total initial displaced volume should be within 5% of the total displaced volume at the end of the computation, i.e., when the initial wave is entirely reflected and offshore.

*Convergence*: The next basic step is checking convergence of the numerical code to a certain asymptotic limit, ideally the actual solution of the equations solved, if one exists. The optimal locations to check convergence are the extreme runup and rundown. The numerical predictions should be seen to converge to a certain value, and further reductions in step sizes should not change the computed results.

## 2.2   Analytical benchmarking

*Why is analytical benchmarking important?* To calculate tsunami currents, forces, and runup on coastal structures and coastal inundation, one must calculate the evolution of the tsunami wave from deep ocean to its target.

Exact solutions of the shallow water-wave equations are useful for validating the complex numerical models that are used for final design. These often involve ad-hoc assumptions, particularly during inundation computations when grid points are introduced and withdrawn as the shoreline recedes and advances. Comparisons of numerical predictions with analytical solutions can identify systematic errors, as when using friction factors or dissipative terms to augment the idealized equations of motion.

Here, we only present certain common 1+1 propagation problems. The

waves evolve over constant-depth and then over plane or composite beaches. Even though most results are derived for idealized waveforms often used in tsunami engineering to describe the leading wave of a tsunami, the generalization to realistic spectral distributions of geophysical tsunamis is trivial with the closed-form integrals provided.

It is important to note that validation should take place with non-periodic waves. During runup, individual monochromatic waves reflect with slope-dependent phase shifts. Whereas a code may model a periodic wave well, it may not model wave superposition well. This was a problem of earlier shallow water-wave formulations that did not account for reflection. While their predictions for the Carrier–Greenspan (Carrier and Greenspan, 1958) sinusoids was correct, they exhibited significant errors when modeling solitary waves or N-waves.

Further, the analytical solutions allow for using cyber-waves of the same scale as geophysical tsunamis. This is in contrast to laboratory experiments that require modeling of small-scale experiments.

Analytical solutions for three problems are presented for analytical benchmarking:

*Single wave on simple beach*: Solitary and N-wave propagation first over the constant-depth then sloping beach is considered. Details of the analytical solutions are given in Appendices A2.1.1, A2.1.2, and A2.1.3. Numerical models should calculate the maximum runup of nonbreaking solitary and N-waves within 5% of the calculated value from the analytical solution. Numerical experiments should be undertaken in a range of depths from 50 cm to 1000 m, and the initial waves scaled appropriately, i.e., for a $\tilde{H}/\tilde{d} = 0.02$ initial solitary wave; at 50 cm the initial height should be 1 cm, at 1000 m it should be 2 m. In addition, the initial value problem solution of the nonlinear shallow water-wave equations is described and runup/rundown and velocity quantities for shoreline are presented in Appendix A2.1.4 for benchmarking. Any well-benchmarked code should produce results within 5% of the calculated value from the analytical solution.

*Solitary wave on composite beach*: 1+1 models that perform well with the solitary wave experiments must still be tested with the composite beach geometry, for which an analytical solution (Appendix A2.2) exists, with solitary waves as inputs. Numerical predictions should not differ by more than 5% in predicting maximum runup for non-breaking waves.

*Subaerial landslide on simple beach*: Inundation computations are exceedingly difficult when the beach is deforming as a landslide is occurring. Numerical predictions of the runup from an idealized landslide of translating Gaussian shaped mass should not differ from the analytical model by more than 10% (Appendix A2.3).

## 2.3   Laboratory benchmarking

*Why is laboratory benchmarking important?* It is quite clear from the earlier discussion that numerical methods have evolved only through careful validation accomplished through comparisons with analytic solutions and laboratory measurements. Long before the availability of numerical codes,

physical models at small scale have been used to visualize wave phenomena in the laboratory and then predictions were scaled to the prototype. Even today, when designing harbors, laboratory experiments—scale model tests— are used to confirm different flow details and validate the numerical model used in the analysis.

For the purpose of validating inundation models, the scale differences are not believed to be important. Numerical codes developed in the last decade that consistently produce predictions in excellent agreement with measurements from small-scale laboratory experiments have been shown to model geophysical-scale tsunamis well. For example, a numerical code that adequately models the inundation in a 1 m-deep model is also expected to model the inundation in the 1 km-deep geophysical geometry, as the grid sizes are adjusted accordingly and in relationship to the scale of the problem. Scale models, in general, do not have bottom friction characteristics similar to real ocean floors or sandy beaches, but this has proven not to be a severe limitation. Tsunamis are such long waves that bottom friction tends to be less important than the inertia of the motion. Friction may be important in cases of extreme inundation, as observed during the 2004 Boxing Day tsunami in Banda Aceh with 3 km inundation distances. However, it has been observed that even with numerical codes that use friction factors within reasonable limits, the predictions are not sensitive to the first order.

Experimental results from five laboratory tests are described as laboratory benchmarking:

*Single wave on simple beach*: Given a small number of 2+1 wave basin laboratory measurements, 1+1 versions of the 2+1 models should be tested with 1+1 directional laboratory models. The solitary wave experiments on the canonical model—waves propagating over a constant-depth region and running up a 1:20 sloping beach—should be used first. Numerical models should calculate the maximum runup of nonbreaking solitary waves within 5% of the measured values in the laboratory. For breaking waves, the models should produce predictions within 10% of the measured values, and they should consistently predict the runup variation described in Appendix A3.1.

*Solitary wave on composite beach*: 1+1 models that perform well with the solitary wave experiments must still be tested with the composite beach geometry (see Appendix A3.2 for details). This additional test will ensure that the code is stable enough for large waves that are near the breaking limit offshore ($\tilde{H}/\tilde{d} = 0.696$). Numerical predictions should not differ by more than 5% from the experimental values, and the numerical procedure should be capable of predicting the entire runup variation.

*Conical island*: 2+1 dimensional calculations should be tested with the conical island geometry of 1:4 slope (Appendix A3.3). The numerical method should stably model two wave fronts that split in front of the island and collide behind it. Predictions of the runup on the back of the island where the two fronts collide should not differ by more than 20% from the laboratory measurements.

*Monai Valley*: 2+1 numerical computations should then be tested with the laboratory model of Monai Valley, Okushiri Island, Japan (Appendix A3.4). The initial condition is a leading depression N-wave, and the entire

simulation shows how well the code performs in a rapid sequence of withdrawal and runup. Comparison of results from different codes has shown that the maximum runup in these experiments can be calculated within 10%, which is thus the standard.

*Landslide*: As discussed, landslide wave generation remains the frontier in terms of numerical modeling, particularly for aerial slides. These involve not only the rapid change of the seafloor, but also the impact of the slide on the shoreline. Therefore numerical codes that will be used to model landslide-generated tsunamis need to be tested against three-dimensional landslide experiments given in Appendix A3.5. It is expected to estimate maximum runup predictions within 10% of the experiments.

## 2.4 Field data benchmarking

*Why is field data benchmarking important?* Verification of a model in a real-world setting is an important part of model validation, especially for operational models. No analytical or laboratory data comparisons (or any limited number of tests, for that matter) can assure robust model performance in the operational environment. Test comparisons with real-world data provide an additional important step in the validation of a model to perform well during operational implementation. The main challenge of testing a model against real-world events is to overcome uncertainties of the tsunami source. While the source of the wave is deterministic in the controlled setting of the laboratory experiment and can be usually reproduced precisely, field data always have uncertainties in the source. For tsunamis, deep ocean measurements are the most unambiguous data quantifying the source of a tsunami.

Only a very limited number of high-quality deep-ocean tsunami measurements exist and these do not include data for Pacific tsunamis that have been destructive or caused inundation (Titov *et al.*, 2005). No DART tsunameters existed in the Indian Ocean at the time of the megatsunami, since DART had only been deployed in the Pacific Ocean. Satellite altimetry measurements of the Indian Ocean tsunami do not provide enough quality and coverage to constrain the tsunami source. Hydrodynamic inversion remains an ill-posed problem and criteria for its regularization are lacking. Deep ocean measurements allow for more defensible inversions, since they are not affected by local coastal effects. Several events have been recorded by both deep-ocean and coastal gages in the Pacific that allow reasonably constrained comparison with models. The expanded DART system array will be providing more tsunami measurements for future events, expanding the library of well-constrained propagation scenarios for testing.

The 10 June 1996 Andreanov Islands (Tanioka and González, 1998) and the 4 October 1994 Kuril Islands (Yeh *et al.*, 1995) events were recorded by several research tsunameters (without real-time data transmission) at similar locations offshore of Alaska and the U.S. West Coast. The offshore model scenario for the Andreanov Island event was obtained from the forecast database by inverting data from research Bottom Pressure Recorders (BPRs) as described in Titov *et al.* (2005). The inversion of the Kuril Islands

data was performed using BPR gages in similar locations. The 17 November 2003 $M_w = 7.8$ Rat Islands tsunami was recorded in real time by the DART tsunameter system and provides a good operational test of field data.

High quality bathymetry/topography data, source definition, and field runup measurements suggest using Okushiri Island, Japan, tsunami data as one of the field benchmarks (Appendix A4.1). In addition, the Rat Islands, Alaska, offshore model scenario constrained by the deep-ocean measurement can be used as input for testing high-resolution inundation models for Hilo Bay, Hawaii, where tide gage recording provides data for model comparison (Appendix A4.2).

*Okushiri Island*: 2+1 computations of the field measurements from the Hokkaido-Nansei-Oki tsunami around Okushiri Island, Japan (Appendix A4.1). The initial condition to be used is DCRC-17a (Takahashi, 1996), which is a composite fault with three segments. The bathymetry and measurements are provided in Appendix A4.1. Predictions for the maximum runup at Aonae, Okushiri Island, Japan, should not differ by more than 20% from the measurements.

*17 November 2003 Rat Islands tsunami*: For operational codes, testing should invert the tsunameter signal of the 17 November 2003 Rat Islands tsunami to improve the initial estimate of sea surface displacement derived from a seismic deformation model, then use the results as input to a Hilo, Hawaii, inundation model to hindcast the tide gage record. This is the most difficult but most realistic test for any operational model, for it involves a forecast (now hindcast) and has to be done much faster than real time. Here, at least the first four waves must be simulated and compared with the observations, with amplitudes and periods accurate to within 25%, maximum amplitude accurate to within 10%, and an arrival time error less than 3 min. Details of the problem are given in Appendix A4.2.

## 2.5   Scientific evaluation

*Peer-review documentation*: Model validation and verification is a continuing process. Any model used for inundation mapping or operational forecasts needs to be presented in peer-reviewed scientific journals with impact factors greater than 0.5. One or more of these publications should include benchmark comparisons identical or similar to those described above.

*Formal scientific evaluation*: A formal evaluation process of individual models needs to be established to avoid ad hoc decisions as to the suitability of any given model. This process may include solicitation of additional reviews of the model's veracity by experts, or the requirement that additional testing be performed. This process will set the standard for the best available practice at any given time, and it will hopefully eliminate the liability to NOAA, universities, states, engineers, and geophysicists who collaborate on the development of inundation maps.

## 2.6 Operational evaluation

The operational evaluation should be done by a test-bed consisting of research and operational parts of NOAA. While the scientific evaluation process may identify models that are realistic and computationally correct, some models may still not be appropriate for operational inundation mapping or forecasting applications. An additional evaluation process must be established to assess a number of model features that bear on important operational factors, such as special implementation hardware/software issues, ease of use, computation time, etc.

Operational evaluation of candidate real-time forecast models should include the following steps:

Step 1—*Meet Operational Forecasting and Inundation Mapping Requirements and Objectives*: Operational requirements include: basic forecasting computation, analysis and visualization tools; integration with operations (vs. separate, stand-alone applications); basic data assimilation techniques; computational resources needed to meet milestones; etc. If a candidate model does not meet specified NOAA forecasting or inundation mapping requirements and objectives, it should be rejected at this point.

Step 2—*Meet Modular Development Requirements*: Various pieces of the forecast model must be developed in parallel based on the overall objectives defined in Step 1.

Step 3—*Meet Test Bed and Model Standards*: In this step, the candidate model is tested against operational standards, with special attention given to the models ability to simulate previous, major tsunamis with the required speed and accuracy. Based on these test results, forecast model development may return to Step 2, proceed, or the candidate model may be rejected for operational use.

Step 4—*Meet Operational Testing Requirements*: The candidate model is integrated into the operational setting for testing. Potential sources are defined and the model is tested in a forecasting mode on an operational platform. Graphical interfaces are developed and forecast models are applied to a few cases to test operational integration and important individual factors such as speed, accuracy, and reliability (see Section 3, below). Operational testing and feedback is provided by the TWCs at this point, and adjustments are made as necessary.

Step 5—*Implement Operationally*: The model is fully integrated into the operational setting and procedures to provide operational products.

## 3. Criteria for Evaluating Operational Forecasting and Inundation Mapping Models

Given the accumulated experience in the tsunami community in the past 50 years, it is now possible to describe the requirements for an ideal tsunami model. Given an earthquake fault mechanism and tsunameter data, the ideal model should accurately predict tsunami inundation of at-risk coastlines in a sufficiently short time. Sufficiently short is defined as the time interval

between the initiation of the tsunami and the calculation of the inundation forecast that allows for evacuation of the target communities. For example, the State of Hawaii needs about 3 hr for a complete and orderly evacuation. An ideal model would accurately forecast inundation at least 3 hr before the tsunami impact is expected anywhere in Hawaii.

What are the requirements for building such an ideal model, and what constraints need to be imposed for model selection and/or further development? The following sections define and provide rationale for these constraints.

## 3.1   Model computational time constraints

The forecast speed will always depend on the distance from the source to the forecast community. However, an ideal forecast would provide a real-time forecast which, after being transmitted to local authorities, allows at least a few minutes before the tsunami impacts the nearest target community. This time interval would allow sirens to trigger the evacuation of beaches and coastal residents and give emergency personnel time to mobilize resources and prepare for search and rescue.

Further, an ideal model would correctly predict the duration of the event. Tsunamis are a series of waves. Tsunamis often get trapped in closed bays or on the continental shelf, resulting in sea level oscillations that may persist for several hours. During the 1993 Okushiri Island, Japan, inundation, bay oscillation at Aonae trapped the tsunami for over 30 min, and a large portion of Aonae remained submerged for a large portion of this time. The Crescent City, California, harbor oscillated for more than 4 hr following the 15 November 2006 tsunami. An operational forecast must ideally provide an estimate of the time that it is safe for search and rescue operations to begin without endangering the lives of responders.

Computational speed standards for inundation maps and real-time forecasts can be different. The current best-practice standard in the U.S. is to use a combination of real-time forecast models at coarse resolution and integrate real-time tsunameter measurements to update the initial sea surface forecast (Titov *et al.*, 2005; Whitmore, 2003). Then a fine-resolution inundation model, developed beforehand and placed on stand-by, ready to be run, uses the output of the fast coarse-resolution computation to produce a quick but physically realistic inundation forecast. The latter is referred to as a Stand-by Inundation Model (SIM).

A long-term forecast for inundation map production is produced months or years before a tsunami strikes; computational time is not the limiting step here. When conducting inundation mapping, the effort is concentrated on acquiring the best available bathymetry/topography and initial conditions to produce the most accurate model results. The objective is to provide guidance for evacuation planning and other hazard assessment products. Inundation mapping is performed at the highest resolution the available resources allow. The current standard is 50 m grid resolution, but site-specific features may demand even finer resolution. Successful computations at resolutions down to 5 m have been performed.

## 3.2 Model accuracy constraints

The accuracy of any given model depends on how well the computational procedure represents the correct solution of the parent equations of motion. When exact solutions exist (as, for example, for certain cases of the linear and nonlinear shallow water-wave equations), the determination of the accuracy of a solution algorithm is straightforward, i.e., through comparisons of the numerical results with the analytical predictions. Determining maximum runup numerically within 5% of the analytical solution is now possible with a handful of models.

For most bathymetries of geophysical interest, analytical solutions do not exist, and it is unlikely that they will ever be determined, due to the complexity of the physical terrain. However, a few laboratory models at smaller scale than the prototype exist: for example, the scale model of Okushiri Island, as described earlier. The Catalina Island, Los Angeles, 2004 model validation workshop of the National Science Foundation identified a handful of models that could predict the laboratory measurements within 10%. While greater compliance with measurements is hoped for in the next decade, 10% accuracy is achievable now and should be considered a standard.

While a numerical model may be validated through comparisons with analytical results and laboratory data, this does not necessarily imply physical realism for tsunamis of geophysical scales. One example is wave breaking. While a numerical model may realistically approximate the solution of the Navier-Stokes equations at laboratory scales, it may not do so at large scales. Calculating the evolution of breaking waves involves calculating turbulent shear terms and invoking turbulence closure constraints which are scale dependent. Therefore a reliability constraint needs to be applied, and this is discussed in the next subsection.

For operational forecast models, propagation accuracy of 5% is now possible (Titov *et al.*, 2005). For inundation models, accuracy of 10% with respect to analytical results and laboratory data is also now possible. Both should be considered as standards.

An associated accuracy constraint is grid resolution. This depends on the complexity of the shoreline. On a fairly plane and very long beach such as those of Southern California, a 100 m grid resolution may be sufficient. The smallest offshore and onshore features likely to affect tsunami impact on a coastal community should be reflected in the numerical grids. If a community is fronted by a sand spit of width 100 m, at least four grid points are needed to provide accurate resolution of the flow over the spit, implying a resolution of less than 25 m. If a coastline is sparsely populated, a 100 m resolution may be sufficient for satisfactory inundation maps, even when the shoreline is complex.

## 3.3 Model reliability and realism constraints

Model reliability refers to how well a given model predicts inundation consistently and realistically from a geophysical point of view. Linear theory may predict wave evolution consistently, but unfortunately not always in

a realistic manner. Linear theory predicts that waves during shoaling will keep growing in height, whereas in reality waves will eventually break, if large enough and when exceeding threshold height-to-depth and height-to-wavelength ratios.

The issue of reliability is crucial. Several numerical models now widely used include ad hoc friction factors. Given that these factors were developed not to model the physical manifestation of frictional dissipation, but simply to stabilize what is by its very nature a marginally stable computation, it is not possible to know a priori how well a model that has been fairly successful in a small number of cases performs in more general cases. For example, a model developed and calibrated for stability with examples from steep coastlines with less than 200 m inundation distances may not perform equally well when employed to forecast the inundation from a tsunami that penetrates more than 3 km inland, as the 26 December 2004 Boxing Day tsunami did in Banda Aceh.

It is clear that any numerical model for inundation predictions needs to be tested over a variety of scales from the laboratory to prototype to ensure both reliability and realism. Ideally, inundation models should be continuously tested with every new set of laboratory data or tsunami field data that becomes available. This will also allow for their further improvement. On the other hand, operational propagation forecasting is by its nature less dependent on scale. Some of the existing methods to test for model accuracy, reliability, and realism are discussed in Appendix A.

## 4.   Summary of Model Evaluation Procedures

State-of-the-art inundation codes in use today have evolved through a painstaking process of careful validation and verification, while operational codes have been developed through extensive verification with measurements from real tsunamis, to the point that every new event poses a diminishing challenge. Mining this experience, procedures for approval and application of numerical models for operational uses are proposed as follows:

1. Establishment of standards for model validation and verification;

2. Scientific evaluation of individual models;

3. Operational evaluation of individual models;

4. Development of operational applications for forecasting;

5. Procedures for transfer of technology to operations.

Only through parallel testing of models under identical conditions, as when there is a tsunami emergency and an operational forecast is performed, can the community determine the relative merits of different computational formulations, an important step to further improvements in speed, accuracy, and reliability.

Figure 1 illustrates the process of model development and evaluation for operational use. The process of operational model development should be
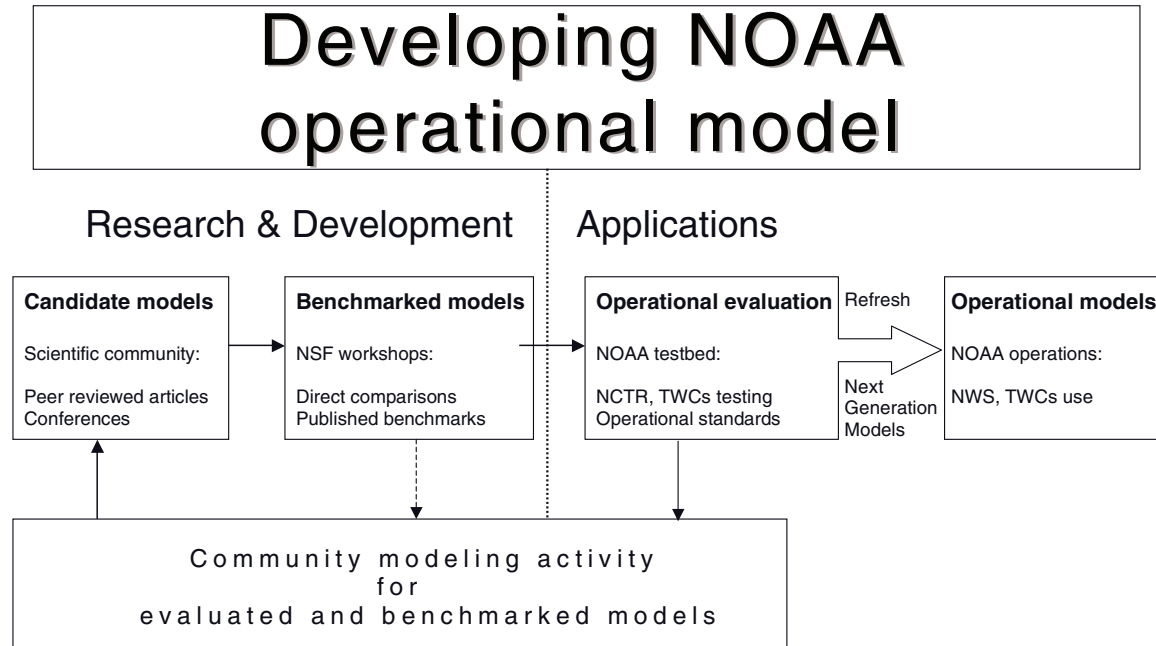
**Figure 1:** Flowchart illustrating the process of NOAA operational model development.

as inclusive as possible, to ensure the active participation of the geophysical, oceanographic, engineering, and NOAA research communities. Currently, scientific evaluation of a tsunami model takes the form of peer-reviewed publications and NSF tsunami model benchmark workshops. NOAA research and operations will evaluate the tsunami model operationally. The Community Modeling Activity will solidify these evaluations into a sustainable developmental effort that will feed NOAA operations with new and refreshed models. NOAA's responsibility is to test benchmarked models for operational suitability to define if a model fits the NOAA operational standards. This evaluation is done by operational and research components of NOAA as a part of the Research-to-Application implementation plan. The models—those that fit NOAA's operational standards—may be implemented for operations. The models that do not fit the standards (due to accuracy, speed, or robustness deficiencies) will stay in the research community modeling activity for improvement and further development.

It is emphasized again that model testing must remain a continuous process. Operational products produced in real time during an actual event must be thoroughly reviewed, and the operational models systematically tested in hindcast mode after each tsunami strikes. The results must be documented and reported to assist the community in developing and implementing improvements, through the identification and resolution of any serious problems or inadequacies of the models and/or products.

While this process may appear onerous, it reflects our state of knowledge as of December 2006, and is the only defensible methodology when human lives are at stake.

# 5.   Acknowledgments

# 6.   References

Borerro, J., M. Ortiz, V.V. Titov, and C.E. Synolakis (1997): Field survey of Mexican tsunami. *Eos Trans. AGU, 78*(8), 85, 87–88 (Eos Cover Article).

Briggs, M.J., C.E. Synolakis, G.S. Harkins, and D. Green (1995): Laboratory experiments of tsunami runup on a circular island. *Pure Appl. Geophys., 144*, 569–593.

Carrier, G.F., and H.P. Greenspan (1958): Water waves of finite amplitude on a sloping beach. *J. Fluid Mech., 17*, 97–110.

Carrier, G.F. (1966): Gravity waves of water of variable depth. *J. Fluid Mech., 24*, 641–659.

Carrier, G.F., T.T. Wu, and H. Yeh (2003): Tsunami runup and drawdown on a sloping beach. *J. Fluid Mech., 475*, 79–99.

Goring, D.G. (1978): Tsunamis—the propagation of long waves onto a shelf. W.M. Keck Laboratory of Hydraulics and Water Resources, California Institute of Technology, Report No. KH-R-38.

Grilli, S.T., I.A. Svenden, and R. Subrayama (1997): Breaking criterion and characteristics of solitary waves on a slope. *J. Waterw. Port Coast. Ocean Eng., 123*(2), 102–112.

Hall, J.V., and J.W. Watts (1953): Laboratory investigation of the vertical rise of solitary waves on impermeable slopes. Tech. Memo. 33, Beach Erosion Board, U.S. Army Corps of Engineers, 14 pp.

Hammack, J.L. (1972): Tsunamis—A model for their generation and propagation. W.M. Keck Laboratory of Hydraulics and Water Resources, California Institute of Technology, Report No. KH-R-28.

Kânoğlu, U. (1998): The runup of long waves around piecewise linear bathymetries. Ph.D. Thesis, University of Southern California, Los Angeles, California, 90089-2531, 273 pp.

Kânoğlu, U. (2004): Nonlinear evolution and runup–rundown of long waves over a sloping beach. *J. Fluid Mech., 513*, 363–372.

Kânoğlu, U., and C.E. Synolakis (1998): Long wave runup on piecewise linear topographies. *J. Fluid Mech., 374*, 1–28.

Kânoğlu, U., and C. Synolakis (2006): Initial value problem solution of nonlinear shallow water-wave equations. *Phys. Rev. Lett., 97*, 148,501–148,504, doi: 10.1103/PhysRevLett.97.148501.

Keller, J.B., and H.B. Keller (1964): Water wave run-up on a beach. ONR Research Report NONR-3828(00), Dept. of the Navy, Wash. DC, 40 pp.

Li, Y., and F. Raichlen (2000): Energy balance model for breaking solitary wave runup. *J. Waterw. Port Coast. Ocean Eng., 129*(2), 47–49.

Li, Y., and F. Raichlen (2001): Solitary wave runup on plane slopes. *J. Waterw. Port Coast. Ocean Eng., 127*(1), 33–44.

Li, Y., and F. Raichlen (2002): Non-breaking and breaking solitary run-up. *J. Fluid Mech., 456*, 295–318.

Liu, P.L.-F., Y.-S. Cho, M.J. Briggs, U. Kânoğlu, and C.E. Synolakis (1995): Runup of solitary waves on a circular island. *J. Fluid Mech., 320*, 259–285.

Liu, P.L.-F., P. Lynett, and C.E. Synolakis (2003): Analytical solutions for forced long waves on a sloping beach. *J. Fluid Mech., 478*, 101–109.

Liu, P.L.-F., C.E. Synolakis, and H.H. Yeh (1991): Report on the International Workshop on Long Wave Runup. *J. Fluid Mech., 229*, 675–688.

Liu, P.L.-F., T.-R. Wu, F. Raichlen, C.E. Synolakis, and J. Borrero (2005): Runup and rundown generated by three-dimensional sliding masses. *J. Fluid Mech., 536*, 107–144.

Liu, P.L.-F., H. Yeh, and C. Synolakis (2007): Advanced Numerical Models for Simulating Tsunami Waves and Runup. *Advances in Coastal and Ocean Engineering, 10*, 250 pp.

National Science and Technology Council (2005): Tsunami Risk Reduction for the United States: A Framework for Action. A Joint Report of the Subcommittee on Disaster Reduction and the United States Group on Earth Observations, 30 pp.

Pedersen, G., and B. Gjevik (1983): Runup of solitary waves. *J. Fluid Mech., 135*, 283–299.

Russel, J.S. (1845): Report on Waves. *Rp. Meet. Brit. Assoc. Adv. Sci. 14th*, 311–390, John Murray, London.

Shuto, N. (1973): Shoaling and deformation of nonlinear waves. *Coastal Eng. Japan, 16*, 1–12.

Synolakis, C.E. (1986): The Runup of Long Waves. Ph.D. Thesis, California Institute of Technology, Pasadena, California, 91125, 228 pp.

Synolakis, C.E. (1987): The runup of solitary waves. *J. Fluid Mech., 185*, 523–545.

Synolakis, C.E., and J.E. Skjelbreia (1993): Evolution of maximum amplitude of solitary waves on plane beaches. *J. Waterw. Port Coast. Ocean Eng., 119*(3) 323–342.

Synolakis, C.E., and E.N. Bernard (2006): Tsunami science before and after Boxing Day 2004. *Phil. Trans. R. Soc. A, 364*(1845), doi: 10.1098/rsta.2006.1824, 2231–2265.

Tadepalli, S., and C.E. Synolakis (1994): The runup of N-waves on sloping beaches. *Proc. R. Soc. Lond. A. 445*, 99–112.

Tadepalli, S., and C.E. Synolakis (1996): Model for the leading waves of tsunamis. *Phys. Rev. Lett., 77*(10), 2141–2144.

Takahashi, T. (1996): Benchmark problem 4; the 1993 Okushiri tsunami—Data, conditions and phenomena. In *Long-Wave Runup Models*, World Scientific, 384–403.

Titov, V.V., and C.E. Synolakis (1995): Modeling of breaking and nonbreaking long-wave evolution and runup using VTCS-2. *J. Waterw. Port Ocean Coast. Eng., 121*(6), 308–316.

Titov, V.V., and C.E. Synolakis (1997): Extreme inundation flows during the Hokkaido–Nansei-Oki tsunami. *Geophys. Res. Lett., 24*(11), 1315–1318.

Titov, V.V., and F.I. González (1997): Implementation and testing of the method of splitting tsunami (MOST). NOAA Technical Memorandum ERL-PMEL-112, PB98-122773, Pacific Marine Environmental Laboratory, Seattle, WA, 11 pp.

Titov, V.V., and C.E. Synolakis (1998): Numerical modeling of tidal wave runup. *J. Waterw. Port Ocean Coast. Eng., 124*(4), 157–171.

Titov, V.V., F.I. González, E.N. Bernard, M.C. Eble, H.O. Mofjeld, J.C. Newman, and A.J. Venturato (2005): Real-time tsunami forecasting: Challenges and solutions. *Nat. Haz., 35*(1), 45–58.

Tuck, E.O., and L.S. Hwang (1972): Long wave generation on a sloping beach. *J. Fluid Mech., 51*, 449–461.

Tanioka, Y., and F.I. González (1998): The Aleutian earthquake of June 10, 1996 (Mw 7.9) ruptured parts of both the Andreanof and Delarof Segments. *Geophys. Res. Lett., 25*(12), 2245–2248.

Whitmore, P.M. (2003): Tsunami amplitude prediction during events: A test based on previous tsunamis. In *Science of Tsunami Hazards, 21*, 135–143.

Yeh H., P.L.-F. Liu, M. Briggs, and C.E. Synolakis (1994): Tsunami catastrophe in Babi Island. *Nature, 372*, 6503–6508.

Yeh, H., P.L.-F. Liu, and C.E. Synolakis (1996): *Long-Wave Runup Models.* World Scientific, 403 pp.

Yeh, H., V.V. Titov, V. Gusyiakov, E. Pelinovsky, V. Khramushin, and V. Kaistrenko (1995): The 1994 Shikotan earthquake tsunami. *Pure Appl. Geophys., 144*(3/4), 569–593.

Zelt, J.A. (1991): The runup of breaking and nonbreaking solitary waves. *Coastal Eng., 125*, 205–246.

# Appendix A: Existing Methods for Model Validation and Verification

Benchmarking of numerical models can be classified into four categories: Basic hydrodynamic considerations, analytical benchmarking, experimental benchmarking, and field benchmarking. Here, specific benchmark problems for validating and verifying computational tools for predicting the coastal effect of tsunamis are described in detail. Some of the benchmark problems described here were used as benchmark problems in the 1995 (Yeh *et al.*, 1996) and 2004 (Liu *et al.*, 2007) Long-Wave Runup Models Workshops in Friday Harbor, Washington, and Catalina Island, Los Angeles, California, respectively.

## 1   Basic hydrodynamic considerations

Two most basic steps are required in ensuring that a numerical model works for predicting evolution and inundation. While the first step is ensuring that the model conserves mass, the second basic step is checking convergence of the numerical code to a certain asymptotic limit.

### *1.1   Mass conservation*

The conservation of mass equation is part of the equations of motion that are solved in any numerical procedure, but cumulative numerical approximations can sometimes produce results that violate mass conservation. This is particularly the case when friction factors are used, or smoothing to stabilize inundation computations for breaking waves.

Conservation of mass can be checked by calculating the water volume at the beginning and at the end of the computation. This should be done by integrating disturbed water depth $\eta(x, y, t)$ over the entire flow domain, i.e., if the flow domain extends from the maximum penetration during inundation $x = X_{max}$ to the outer location of the source region $X_S$, and $y = Y_{max}$ to $Y_S$, then total displaced volume $V(t)$ is

$$V(t) = \int_{X_{max}}^{X_S} \int_{Y_{max}}^{Y_S} \eta(x, y, t) dx dy. \tag{A1}$$

The integral of $\eta(x, y, t)$ should be used instead of the integral of the entire flow depth $h(x, y, t) = \eta(x, y, t) + d(x, y, t)$—where $d(x, y, t)$ is the undisturbed water depth—because the latter is likely to conceal errors in the calculation. Typically, $\eta \ll d$ at offshore integrating $h$ will simply produce the entire volume of the flow domain and will mask errors. Note that testing of the conservation of mass as above involves placing a closed domain within reflective boundaries.

Numerical models use absorbing boundaries to allow the wave to radiate outwards. While some loss of mass may in theory occur due to the differencing at the boundary, placing the computational boundaries far enough from the source ensures this loss is minimal. Nonetheless, testing conservation

of mass with open boundaries and monitoring the volume fluxes over the corresponding boundaries at $x = x_b$ and $y = y_b$ is computationally possible. The net flux needs to be added or subtracted to the total displaced volume.

The calculation of the entire volume of the wave motion of the flow domain at the beginning and end of the computation—to ensure that mass is conserved—is very important in code validation. Once the associated mass fluxes at the boundaries are considered, numerical errors can be highly additive, and mass invariably decreases in numerical computations. It is essential that codes self-monitor the entire volume; if the difference between start and finish is greater than 5%, the grid needs to be readjusted. Usually with few changes in $\Delta x$, $\Delta y$, and $\Delta t$, the conservation of mass can be improved.

Calculations of conservation of mass should be such that the total initial displaced volume $V(t = 0)$ should be within 5% of the total displaced volume at the end of the computation $V(t = T)$ where $T$ represents the computation end time. It is assumed that the end of the computation is when the initial wave is entirely reflected and offshore.

### 1.2   Convergence

The next basic step is checking convergence of the numerical code to a certain asymptotic limit, presumably the actual solution of the equations solved. The grid steps $\Delta x$ and $\Delta y$ need to be halved, and the time step $\Delta t$ reduced appropriately to conform with the Courant–Friedrics–Levy (CFL) criterion. The optimal locations to check convergence are the extreme runup and rundown. A graph needs to be prepared presenting the variation of the calculated runup and rundown (ordinate) with the step size (abscissa). As the step size is reduced, the numerical predictions should be seen to converge to a certain value, and further reductions in step size should not change the results.

## 2   Analytical benchmarking

The shallow water-wave (SW) equations describe the evolution of the water-surface elevation and of the depth-averaged water particle velocity of waves with wavelengths large compared with the depth of propagation. The equations assume that the pressure distribution is hydrostatic everywhere, i.e., there is no variation with depth of any of the other flow variables. In this section we present several analytic solutions to the 1+1 version of these equations. As stated in Section 2 of this report, 1+1 models are generally unreliable for inundation mapping and entirely inadequate for operational tsunami forecasting, but they are invaluable to the process of testing and validating models.

### 2.1   Single wave on a simple beach

The so-called canonical problem of the shallow water-wave equations is the calculation of a long wave climbing up a sloping beach of angle $\beta$ coupled to a constant-depth region (Fig. A1). The origin of the coordinate system is at
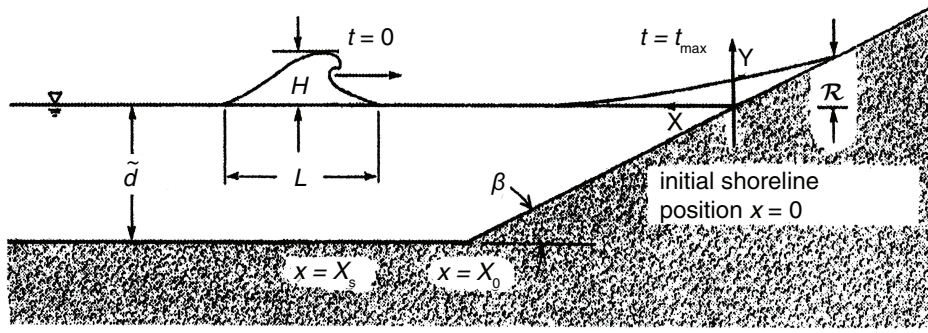
**Figure A1:** Definition sketch for canonical bathymetry, i.e., sloping beach connected to a constant-depth region.

the initial position of the shoreline and $x$ increases seaward. Dimensionless variables are introduced as follows:

$$x = \frac{\tilde{x}}{\tilde{d}}, \quad (\eta, \ h_0) = \frac{(\tilde{\eta}, \ \tilde{h}_0)}{\tilde{d}}, \quad u = \frac{\tilde{u}}{\sqrt{\tilde{g}\tilde{d}}}, \quad \text{and} \ \ t = \frac{\tilde{t}}{\sqrt{\tilde{d}/\tilde{g}}}. \tag{A2}$$

Here quantities with tilde are dimensional and $\eta$ is the amplitude, $u$ is the depth-averaged horizontal velocity, $h_0$ is the undisturbed water depth, $\tilde{d}$ is the depth of the constant-depth region, and $\tilde{g}$ is the gravitational acceleration. The topography is described by $h_0(x) = x \tan \beta$ when $x \leq X_0 = \cot \beta$ and $h_0(x) = 1$ when $x \geq X_0 = \cot \beta$. Even though dimensionless variables are not preferred in engineering practice, here they have distinct advantages as everything scales simply with an offshore characteristic depth. In numerical solutions, dimensional variables are most often used.

Consider a tsunami evolution problem described by the $1 + 1$ nonlinear shallow water-wave (NSW) equations:

$$\begin{aligned} h_t + (uh)_x &= 0, \\ u_t + uu_x + \eta_x &= 0, \end{aligned} \tag{A3}$$

with $h(x,t) = \eta(x,t) + h_0(x)$. Through elementary manipulations, neglecting nonlinear terms, (A3) reduces to

$$\eta_{tt} - (\eta_x h_0)_x = 0, \tag{A4}$$

an equation known as the linearized shallow water-wave (LSW) equation. Over constant-depth $h_0 = 1$, then

$$\eta_{tt} - \eta_{xx} = 0, \tag{A5}$$

the classic one-dimensional wave equation.

The solution follows directly from the Fourier transform of the equation when a boundary condition for the wave amplitude $\eta(X_1, t)$ is specified, i.e.,

when the incident wave $\eta(x, t)$ at the constant-depth region is known at some $x = X_1$, and can be described by a Fourier integral of the form

$$\eta(X_1, t) = \int_{-\infty}^{+\infty} \Phi(\omega) e^{-i\omega t} d\omega. \tag{A6}$$

Consider the canonical problem of a constant-depth region of depth $h_0 = 1$ joined to a sloping beach of angle $\beta$, with the toe of the beach at $x = X_0$. Synolakis (1986, 1987) matched the linear theory solution at the constant-depth with the solution over the sloping beach as derived by Keller and Keller (1964) to derive the solution over the sloping beach for a wave with a transform as given by (A6),

$$\eta(x, t) = 2 \int_{-\infty}^{+\infty} \Phi(\omega) \frac{J_0(2\omega\sqrt{xX_0}) e^{-i\omega(X_0 + t)}}{J_0(2X_0\omega) - iJ_1(2X_0\omega)} d\omega, \tag{A7}$$

where $X_0 = \cot\beta$. This solution is only valid when $0 \leq x \leq X_0$; when $x < 0$, (A4) does not reduce to Bessel's equation. Notice that the integral (A7) can be evaluated with standard numerical methods; however, the advantage of this form is that it allows calculation of the solution for many physically realistic tsunami waveforms simply by plugging in the $\Phi(\omega)$ of the incoming wave, hopefully known at some offshore location $X_1$.

**2.1.1  Solitary wave evolution and runup**  As discussed in Synolakis (1986, 1987) it is possible to derive exact results for the evolution and runup of solitary waves based on linear theory. Solitary waves have long been used as a model for the leading wave of tsunamis. Solitary waves were first described by Russel (1845) as the great waves of translation, and consist of a single elevation wave. While capturing some of the basic physics of tsunamis, they do not model the physical manifestation of tsunamis in nature, which are invariably N-wave like with a leading-depression wave followed by an elevation wave. A solitary wave centered offshore at $x = X_s$ at $t = 0$ has the following surface profile,

$$\eta(x, 0) = H \text{sech}^2 \gamma(x - X_s), \tag{A8}$$

where $\gamma = \sqrt{3H/4}$ and $H$ is the dimensionless wave height, i.e., $H = \widetilde{H}/\widetilde{d}$. The function $\Phi(\omega)$ associated with this profile is derived in Synolakis (1986) and it is given by:

$$\Phi(\omega) = \frac{2}{3}\omega \text{cosech}(\alpha\omega) e^{i\omega X_s}, \tag{A9}$$

where $\alpha = \pi/(2\gamma)$.

In the context of water-wave theory, the solitary wave (A8) is an exact solution of the Korteweg-de-Vries (KdV) equation; therefore, a KdV solitary wave propagates over constant-depth without any change in shape. The KdV theory is both dispersive and nonlinear, and solitary waves are the only waves with this unique property of unchanging shape. However, (A8) can be used as an initial condition for other wave theories, without, of course, a priori expectation that the SW model will preserve the classic

soliton properties, which include their ability to go through each other (interact) without any change in shape through nonlinear interactions. This having been said, since the LSW is nondispersive and linear, hence all waves propagate over constant-depth without any change in shape. However, in the range of wave steepness and amplitudes relevant for tsunamis, it is now well established that, at least for the $1 + 1$ problem far from the shoreline, the LSW theory, which also preserves the wave shape for propagation over constant-depth, is quite adequate (Liu *et al.*, 1991) and useful when the engineering problem has simple geometry.

The derivation of the amplitude evolution for solitary waves is not as straightforward as often assumed. When superposing sinusoids, there is a frequency $\omega$-dependent phase shift. It is therefore not obvious that linear superposition will produce a similar amplitude variation given this frequency-dependent phase shift.

To describe the evolution of a solitary wave up a plane beach, Synolakis (1986, 1987), substituted (A9) into (A7) to obtain

$$\eta(x,t) = \frac{4}{3} \int_{-\infty}^{+\infty} \omega \operatorname{cosech}(\alpha\omega) \frac{J_0(2\omega\sqrt{xX_0})e^{-i\omega(X_0 - X_s + t)}}{J_0(2X_0\omega) - iJ_1(2X_0\omega)} d\omega, \qquad \text{(A10)}$$

where, as earlier, $\alpha = \pi/\sqrt{3H}$. This integral can be evaluated directly through contour integration. In the region where the wave evolves on the sloping beach far off the shoreline, $x$ is large, and (A10) becomes

$$\eta(x,t) = \frac{4\pi^2}{3\alpha^2}\left(\frac{X_0}{x}\right)^{1/4} \sum_{n=1}^{+\infty}(-1)^{n+1}ne^{-(\pi/a)\theta' n}, \qquad \text{(A11)}$$

with $\theta' = X_0 - X_s - t - 2\sqrt{xX_0}$. The maximum of the power series is $1/4$, therefore the maximum local value of the wave amplitude $\eta_{\max}$ is given explicitly by

$$\frac{\eta_{\max}}{H} = \left(\frac{X_0}{x}\right)^{1/4} = \left(\frac{1}{h_0}\right)^{1/4}; \qquad \text{(A12)}$$

this is an amplitude variation similar to Green's law.

The region over which (A12) applies is the region of gradual shoaling; the region of rapid shoaling is often identified with the Boussinesq result, i.e., $\eta_{\max} \sim h$. The fact that both evolution laws may coexist was first identified by Shuto (1973). Synolakis and Skjelbreia (1993) also present results which show that Green's law type evolution is valid over a wide range of slopes and for finite-amplitude waves at least in the region of gradual shoaling.

The results (A10) can now be readily applied to derive a result for the maximum runup of a solitary wave climbing up a sloping beach. Writing $R(t) = \eta(0,t)$, i.e., $R(t)$ is the free-surface elevation at the initial shoreline; in the LSW theory, the shoreline does not move beyond $x = 0$. The maximum value of $R(t)$ is the maximum runup $\mathcal{R}$, arguably the most important parameter in the long-wave runup problem, and it is the maximum vertical excursion of the shoreline. Per Synolakis (1986), from equation (A10), it can

be deduced that

$$R(t) = 8H \sum_{n=1}^{+\infty} \frac{(-1)^{n+1} n e^{-2\gamma(X_s - X_0 - t)n}}{I_0(4\gamma X_0 n) + I_1(4\gamma X_0 n)}. \tag{A13}$$

The series can be simplified further by using the asymptotic form for large arguments of the modified Bessel functions. The resulting series is of the form $s = \sum_{n=1}^{\infty} (-1)^{n+1} n^{3/2} \chi^n$; its maximum value $s_{\max}$ occurs at $\chi = 0.481 = e^{-0.732}$ with $s_{\max} = 0.15173$. Then the following expression results for the maximum runup $\mathcal{R}$:

$$\mathcal{R} = 2.831 \sqrt{\cot \beta} H^{5/4}. \tag{A14}$$

This result is formally correct when $\sqrt{H} \gg 0.288 \tan \beta$—the assumption implied when using the asymptotic form of the Bessel functions. Equation (A14) was first derived by Synolakis (1986) and has since been referred to as *the runup law* and shown in Fig. A2. As will be apparent in later sections, this methodology is quite powerful to find the maximum runup and it allows calculation of the runup of other waveforms such as N-waves, not to mention the runup of waves evolving over piecewise-linear bathymetries. Recent results suggest that the dependence of the runup on the slope and on the offshore wave height in a two-dimensional problem of idealized conditions is often quite similar to this one-dimensional power law.

The asymptotic result (A14) is valid for waves that do not break during runup, suggesting that it is appropriate to use the qualifier nonbreaking for waves that do not break during runup but may or may not break during rundown. The real usefulness of any asymptotic result is how well it identifies the scaling, i.e., it can identify the solution dependence on the problem parameters; numerical solutions will invariably produce more accurate specific predictions, but they can rarely provide useful information about the problem scaling. To check if the runup law (A14) provides the correct scaling, Synolakis (1986, 1987) examined the classic laboratory data set of Hall and Watts (1953), Fig. A2. That study includes both breaking and nonbreaking wave data without identifying them as such, clearly because there was no realization of the differences; the empirical runup relationships derived by Hall and Watts (1953) are not directly applicable when determining the runup of nonbreaking waves. To perform a posteriori identification of those data, the breaking criterion $H < 0.479(\cot \beta)^{-10/9}$ was used.

**2.1.2   N-wave runup**   Most tsunami eyewitness accounts suggest that tsunamis are N-wave like, i.e., they are dipolar, which means they appear as a combination of a depression and an elevation wave, and frequently as a series of N-waves, sometimes known as double N-waves. Up until the late 1990s, the solitary wave model was used exclusively to evaluate the runup of tsunamis. The N-wave model was motivated by observations from earthquakes in Nicaragua [1 September 1993], Flores, Indonesia [12 December 1992], Okushiri, Japan [7 July 1993], East Java, Indonesia [6 June 1994], Kuril Islands, Russia [4 October 1994], Mindoro, Philippines [14 November 1994], Manzanillo, Mexico [9 October 1995], Chimbote, Peru [3 March 1996], Papua New Guinea [17 July 1998], Vanuatu [26 November 1999], and
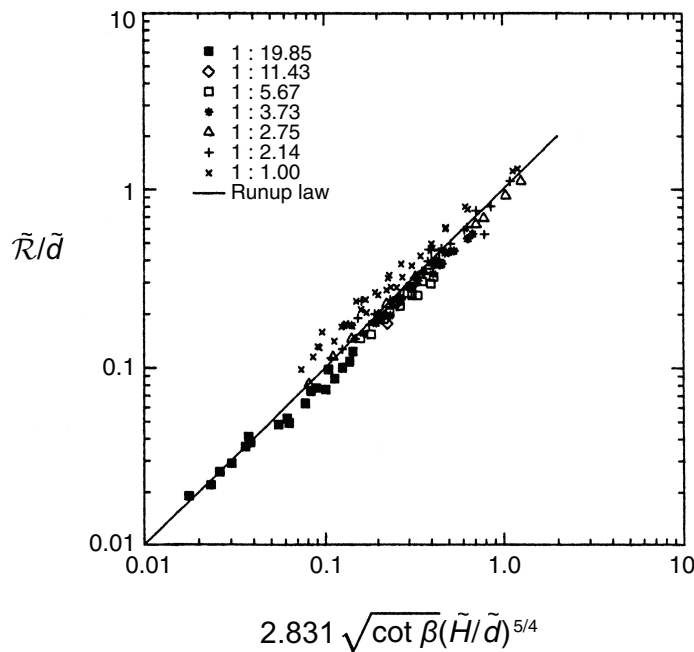
**Figure A2:** Laboratory data for maximum runup of nonbreaking waves climbing up different beach slopes: ■ 1:19.85 (Synolakis, 1986), ◊ 1:11.43 (Hall and Watts, 1953), □ 1:5.67 (Hall and Watts, 1953), ∗ 1:3.73 (Hall and Watts, 1953), △ 1:2.75 (Pedersen and Gjevik, 1983), + 1:2.14 (Hall and Watts, 1953), × 1:1.00 (Hall and Watts, 1953). Solid line represents the runup law (A14).

Caminade, Peru [20 June 2001], all of which produced tsunami waves which caused nearby shorelines to first recede before advancing. The most specific description was during the 9 October 1995 Manzanillo, Mexico earthquake. One eyewitness saw the shoreline retreat beyond a rock outcrop which was normally submerged in over 5 m depth and at a distance of about 400 m from the shoreline, suggesting a leading-depression wave. Before the megatsunami of 26 December 2004, this was the only photographic evidence of these leading-depression waves (Borrero *et al.*, 1997). Recall that the megatsunami manifested itself first with a rapid withdrawal of the water surface in most locales east of the rupture zone.

Modeling tsunamis with solitary waves cannot possibly explain these observations, because a solitary wave is technically a leading-elevation wave. Therefore, and to reflect the fact that tsunamigenic faulting in subduction zones associated with both vertical uplift and subsidence of the sea bottom, Tadepalli and Synolakis (1994) conjectured that all tsunami waves at generation have an N-wave or dipole shape. Tadepalli and Synolakis (1994, 1996) proposed a general function as a unified model for both near-shore and far-field tsunamis as generalized N-waves. When a wave propagates with the trough first it is referred to as a leading depression N-wave or LDN. When the crest arrives first, it is a leading-elevation wave or LEN. Also, Tade-

palli and Synolakis (1994) defined another type of N-wave of this class with leading-elevation and depression waves of the same height and at a constant separation distance and refer to this wave as an isosceles N-wave with a surface profile given by

$$\eta(x,0) = \frac{3\sqrt{3}H}{2}\text{sech}^2[\gamma(x-X_N)]\tanh[\gamma(x-X_N)], \qquad (A15)$$

with $\gamma = \frac{3}{2}\sqrt{\sqrt{\frac{3}{4}}H}$. Wave profile (A15) is an LDN and has a maximum wave amplitude $H$. The function $\Phi(\omega)$ associated with this profile is derived in Tadepalli and Synolakis (1994) using contour integration and it is given by:

$$\Phi(\omega) = \frac{2i}{3\gamma}\omega^2\text{cosech}(\frac{\pi\omega}{2\gamma})e^{i\omega X_N}. \qquad (A16)$$

Now, the maximum of $R(t) = \eta(0,t)$ can be evaluated for LEN using the symmetry of the profile given in (A15) and one can find that

$$\mathcal{R}_{\text{N-wave}} = 3.86\sqrt{\cot\beta}H^{5/4}. \qquad (A17)$$

Comparing the runup of the Boussinesq solitary wave (A14) with the runup of an isosceles N-wave, $\mathcal{R}_{\text{N-wave}} = 1.364\mathcal{R}_{\text{Solitary}}$. Because of the symmetry of the profile, this is also the minimum rundown of an isosceles leading-depression N-wave. Tadepalli and Synolakis (1994) showed that the normalized maximum runup of nonbreaking isosceles LEN is smaller than the runup of isosceles LDN, and that both are higher than the runup of a solitary wave with the same wave height, and the latter is known as the N-wave effect (Fig. A3).

The two-dimensional character of the generation region limits the direct application of the N-wave and solitary wave models. However, N-wave theory does provide a conceptual framework for analysis and for explaining certain field observations qualitatively.

**2.1.3  Boundary value problem**  To solve the nonlinear set (A3) for the sloping beach case, $h_0(x) = x\tan\beta$, Carrier and Greenspan (1958) introduced the hodograph transformation known as Carrier–Greenspan transformation:

$$u = \frac{\psi_\sigma}{\sigma}, \qquad (A18)$$

$$\eta = \frac{\psi_\lambda}{4} - \frac{u^2}{2}, \qquad (A19)$$

$$t = \cot\beta(\frac{\psi_\sigma}{\sigma} - \frac{\lambda}{2}), \qquad (A20)$$

$$x = \cot\beta(\frac{\sigma^2}{16} - \frac{\psi_\lambda}{4} + \frac{u^2}{2}), \qquad (A21)$$

into (A3), and they derived the following second-order ordinary differential equation:

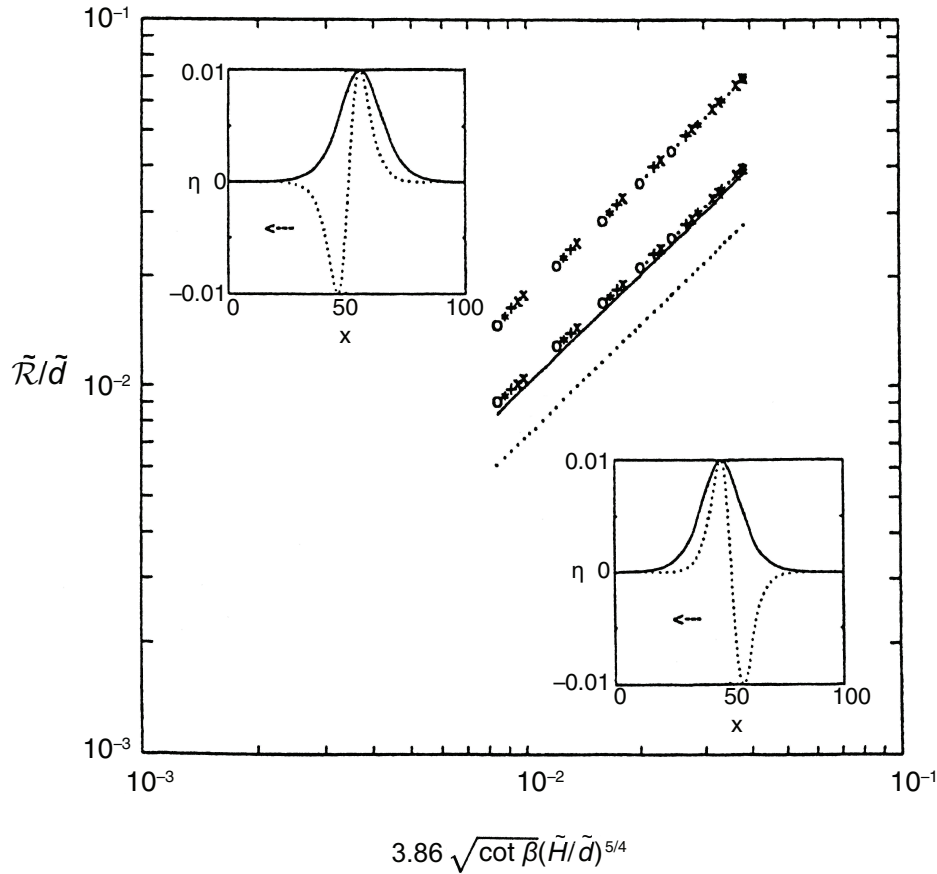$$(\sigma\psi_\sigma)_\sigma = \sigma\psi_{\lambda\lambda}. \qquad (A22)$$

**Figure A3:** Maximum runup of isosceles N-waves and solitary wave. Top and lower set of points are results for the maximum runup of leading-depression and -elevation isosceles N-waves, respectively. Dotted line represents the runup of solitary wave (A14). Lower and upper insets compare a solitary wave profile to a leading-depression and -elevation isosceles N-waves, respectively.

Note that the original Carrier–Greenspan transformation does not include $\cot\beta$ in (A20) and (A21) because of a different scaling as given in (A25) in section A2.1.4. Note also the similarity with the linear form of the shallow water-wave equation (LSW), $(\eta_x h_0)_x = \eta_{tt}$. Also, notice the conservation of difficulty. Instead of having to solve the coupled nonlinear set (A3), one now has to solve a linear equation, but the transformation equations which relate the transformed variables with the physical variables are nonlinear, coupled, and implicit. Yet, a redeeming feature is that in the hodograph plane, i.e., in the $(\sigma, \lambda)$-space, the shoreline is always at $\sigma = 0$. This allows for direct analytical solutions without the complications of the moving shoreline boundary.

In general, it is quite difficult to specify initial or boundary data for the nonlinear problem in the physical $(x, t)$-space coordinates without making restrictive assumptions; a boundary condition requires specification of the solution at $(X_0, \forall t)$, and an initial condition specification at $(t_0, \forall x)$, but, in

practice, the wave approaching the beach is only known offshore for $(X_0 \geq \cot \beta, t < t_0)$, where $t_0$ is the time that the wave reaches the $x$-location $X_0$. Even when boundary or initial conditions are available in the $(x,t)$-space, the process of deriving the equivalent conditions in the $(\sigma, \lambda)$-space is not trivial.

These difficulties have restricted the use of this transformation to problems that can be reduced directly to those solved by Carrier and Greenspan (1958). Synolakis (1986) revived the Carrier–Greenspan formalism by developing a method to specify a boundary condition including reflection. Synolakis (1986) used the solution of the equivalent linear problem, as given by (A7), at the seaward boundary of the beach, i.e., at $x = X_0 = \cot \beta$ corresponding to $\sigma = \sigma_0 = 4$. Then, equation (A19) implies that $\eta(X_0, t) \approx \frac{1}{4}\psi_\lambda(4, \lambda)$. Assuming that $\psi(\sigma_0, \lambda) \to 0$ as $\lambda \to \pm\infty$, Synolakis (1986, 1987) showed that the Carrier–Greenspan potential is given by

$$\psi(\sigma, \lambda) = -\frac{16i}{X_0} \int_{-\infty}^{+\infty} \frac{\Phi(\kappa)}{\kappa} \frac{J_0(\sigma\kappa X_0/2)e^{-i\kappa X_0(1-\frac{\lambda}{2})}}{J_0(2\kappa X_0) - iJ_1(2\kappa X_0)} d\kappa. \tag{A23}$$

Even though the solution now can be obtained in the $(\sigma, \lambda)$-space using (A18) and (A19) and can be converted to the solution in the $(x,t)$-space through (A20) and (A21), the problem with this transformation is deriving a solution for a particular-time $t^*$ or at a particular-location $x^*$. Synolakis (1986) and later Kânoğlu (2004) evaluated the solution either for given $t^*$ or at given $x^*$ using the Newton–Raphson iteration algorithms, respectively;

$$\lambda_{i+1} = \lambda_i - \left[ \frac{t^* - t(\lambda)}{\frac{\partial}{\partial \lambda}\left[t^* - t(\lambda)\right]} \right]_{\lambda_i} \quad \text{or} \quad \sigma_{i+1} = \sigma_i - \left[ \frac{x^* - x(\sigma)}{\frac{\partial}{\partial \sigma}\left[x^* - x(\sigma)\right]} \right]_{\sigma_i}.$$

$$(A24a, b)$$

Here $t(\lambda)$ and $x(\sigma)$ are given with (A20) and (A21), respectively.

An astonishing feature of the NSW is that the predictions for the maximum runup are identical to those of the LSW, when identical boundary conditions are specified at $X_0 = \cot \beta$. The maximum runup according to LSW is the maximum value attained by the wave amplitude at the initial position of the shoreline, while the maximum runup is given by the maximum value of the amplitude at the evolving shoreline $\eta(x_s, \lambda)$, where $x_s$ is the $x$-coordinate of the shoreline tip and corresponds to $\sigma = 0$. Carrier (1966)—without reflection—and Synolakis (1987)—including reflection—have shown that the linear and nonlinear theory produce mathematically identical predictions. Nonlinear analytical evolution of solitary wave with $H = 0.0185$ over a sloping beach of 1:19.85 is given in Fig. A4.

**2.1.4   *Initial value problem***   The nonlinear evolution of a wave over a sloping beach is theoretically and numerically challenging due to the moving boundary singularity. Yet, it is important to have a good estimate of the shoreline velocity and associated runup–rundown motion, since they are crucial for the planning of coastal flooding and of coastal structures. As explained in the previous section, Synolakis (1987) solved this problem as a boundary value problem considering canonical bathymetry. Kânoğlu (2004)
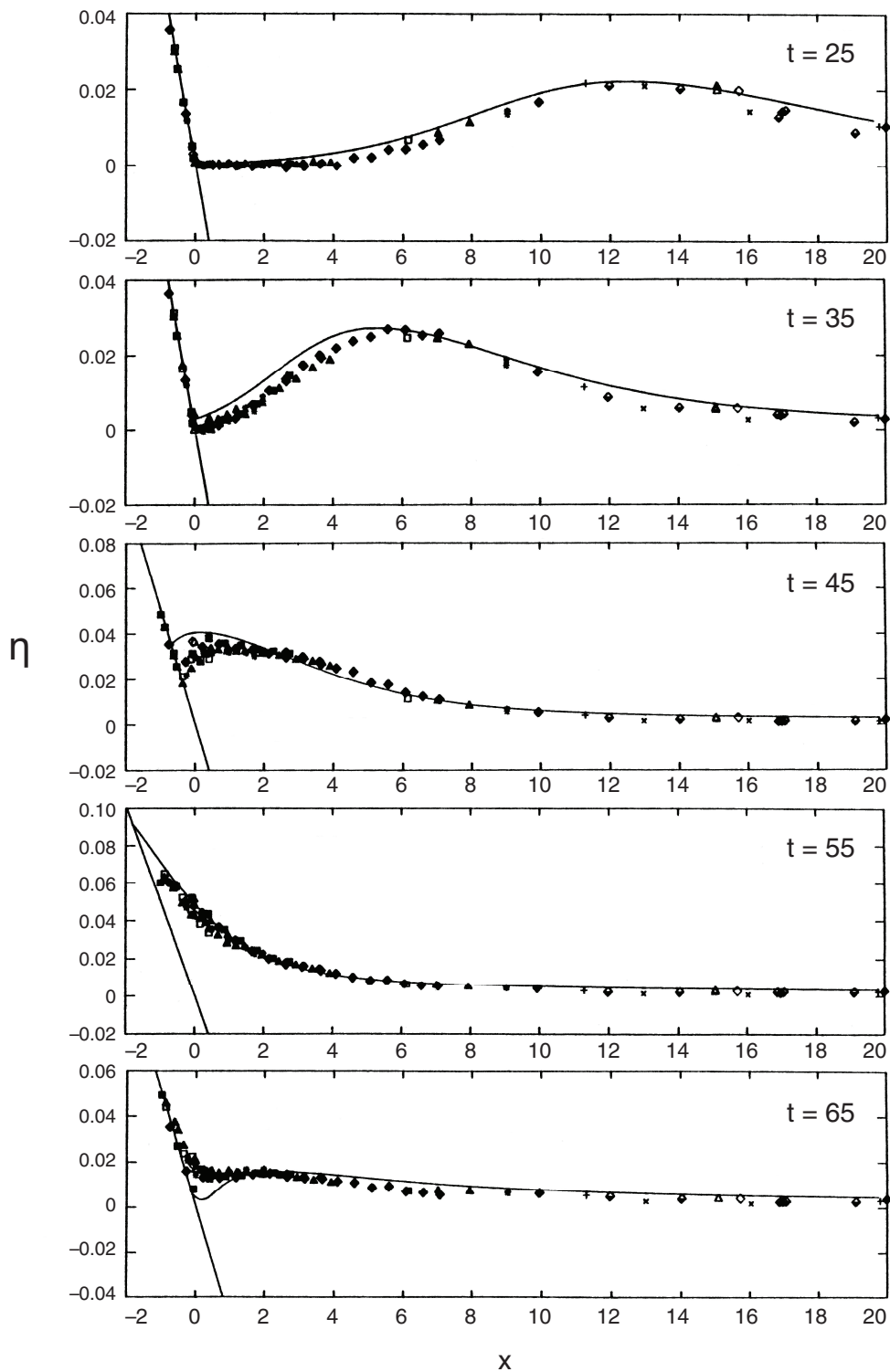
**Figure A4:** Time evolution of $H = 0.0185$ initial wave over a sloping beach with $\cot\beta = 19.85$ from $t = 25$ to 65 with 10 increments. Constant depth-segment starts at $X_0 = 19.85$. While markers show experimental results of Synolakis (1986, 1987), solid lines show nonlinear analytical solution of Synolakis (1986, 1987).
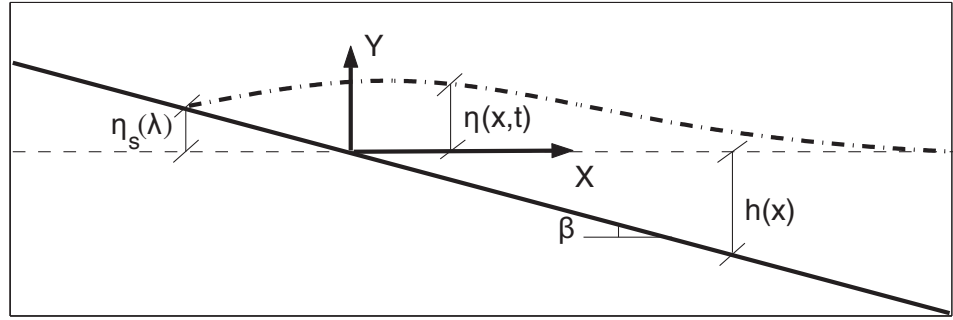
**Figure A5:** Definition sketch for the initial value problem.

solved nonlinear evolution of any given wave form over a sloping beach as an initial value problem (Fig. A5). It is proposed that any initial waveform can first be represented in the transform space using the linearized form of the Carrier–Greenspan transformation for the spatial variable, then the nonlinear evolutions of these initial waveforms can be directly evaluated. Later, Kânoğlu and Synolakis (2006) solved the similar problem considering a more general initial condition, i.e., initial wave with velocity.

Kânoğlu (2004) considers NSW equations (A3) with slightly different nondimensionalization than (A2), i.e., using the reference length $\widetilde{l}$ as a scaling parameter, the dimensionless variables are introduced as

$$x = \frac{\widetilde{x}}{\widetilde{l}}, \ \ (h, \ \eta) = \frac{(\widetilde{h}, \ \widetilde{\eta})}{\widetilde{l}\tan\beta}, u = \frac{\widetilde{u}}{\sqrt{\widetilde{g}\,\widetilde{l}\tan\beta}}, \ \ \text{and} \ \ t = \frac{\widetilde{t}}{\sqrt{\widetilde{l}/(\widetilde{g}\,\tan\beta)}} \ . \quad (A25)$$

Using the original Carrier–Greenspan transformation—without $\cot\beta$ coefficient in (A20) and (A21)—it is possible to reduce the NSW equations to the following single second-order linear equation the same as (A22):

$$\sigma\phi_{\lambda\lambda} - (\sigma\phi_\sigma)_\sigma = 0, \quad (A26)$$

using the Riemann invariants of the hyperbolic system (Carrier and Greenspan, 1958). The Carrier–Greenspan transformation not only reduces the nonlinear shallow water-wave equations into a second-order linear equation, but also fixes the instantaneous shoreline to $\sigma = 0$ in the $(\sigma, \lambda)$-space as explained previously. Furthermore, a bounded solution at the shoreline combined with a given initial condition in terms of a wave profile at $\lambda = 0$ in the $(\sigma, \lambda)$-space, $\eta(\sigma, 0)$ implies the following solution in the transform space,

$$\phi(\sigma, \lambda) = -\int_0^\infty \int_0^\infty \frac{1}{\omega}\xi^2\Phi(\xi)J_0(\omega\sigma)J_1(\omega\xi)\sin(\omega\lambda)\mathrm{d}\omega\mathrm{d}\xi, \quad (A27)$$

where $\Phi(\sigma) = u_\lambda(\sigma, 0) = 4\eta_\sigma(\sigma, \ 0)/\sigma$. Further, given the initial waveform

$\eta(\sigma, 0)$, the evolution of the water-surface elevation is now given by

$$\eta(\sigma, \lambda) = \frac{1}{4}\phi_\lambda - \frac{1}{2}u^2$$

$$= -\frac{1}{4}\left\{\int_0^\infty \xi^2\Phi(\xi)\left[\int_0^\infty J_0(\omega\sigma)J_1(\omega\xi)\cos(\omega\lambda)d\omega\right]d\xi\right\}$$

$$-\frac{1}{2}\left\{\int_0^\infty \xi^2\Phi(\xi)\left[\int_0^\infty \frac{J_1(\omega\sigma)}{\sigma}J_1(\omega\xi)\sin(\omega\lambda)d\omega\right]d\xi\right\}^2 \quad \text{(A28)}$$

where, again, $\Phi(\sigma) = 4\,\eta_\sigma(\sigma, 0)/\sigma$.

Since it is important for coastal planning, simple expressions for shoreline runup–rundown motion and velocity are useful. Considering the shoreline corresponds to $\sigma = 0$ in the $(\sigma, \lambda)$-space, (A28) reduces to the following equation for the runup–rundown motion:

$$\eta_s(\lambda) = \eta(0, \lambda) = \frac{1}{4}\phi_\lambda - \frac{1}{2}u_s^2$$

$$= -\frac{1}{4}\left\{\int_0^\infty \xi^2\Phi(\xi)\left[\int_0^\infty J_1(\omega\xi)\cos(\omega\lambda)d\omega\right]d\xi\right\}$$

$$-\frac{1}{2}\left\{\int_0^\infty \xi^2\Phi(\xi)\left[\int_0^\infty \frac{1}{2}\omega J_1(\omega\xi)\sin(\omega\lambda)d\omega\right]d\xi\right\}^2. \quad \text{(A29)}$$

Here $u_s$ and $\eta_s$ represent shoreline velocity and motion, respectively. The singularity of the $u = \phi_\sigma/\sigma$ at the shoreline ($\sigma = 0$) is removed with the consideration of the $\lim_{\sigma\to 0}\left[J_1(\omega\sigma)/\sigma\right] = \frac{1}{2}\omega$.

The difficulty of deriving an initial condition in the $(\sigma, \lambda)$-space is overcome by simply using the linearized form of the hodograph transformation for a spatial variable in the definition of initial condition. It is proposed that any initial waveform can first be represented in the transform space using the linearized form of the Carrier–Greenspan transformation for the spatial variable ((A21) without $\cot\beta$ coefficient), then the nonlinear evolutions of these initial waveforms can be directly evaluated. Once an initial value problem is specified in the $(x, t)$-space as $\eta(x, 0)$, the linearized hodograph transformation $x \cong \frac{1}{16}\sigma^2$ is used directly to define the initial waveform in the $(\sigma, \lambda)$-space, $\eta(\frac{1}{16}\sigma^2, 0)$. Thus $\Phi(\sigma) = 4\eta_\sigma(\frac{1}{16}\sigma^2, 0)/\sigma$ is found, and $\phi(\sigma, \lambda)$ follows directly through a simple integration, as in (A28). Then it becomes possible to investigate any realistic initial waveform such as Gaussian and N-wave shapes employed in Carrier *et al.* (2003) and the isosceles and general N-waves defined by Tadepalli and Synolakis (1994). Again, solution in the physical space can be found using the Newton–Raphson algorithm proposed by Synolakis (1987) and later used by Kânoğlu (2004), as presented in (A24a, b).

The shoreline runup-rundown motion and velocity are presented for one of the initial profiles given by Carrier *et al.* (2003):

$$\eta(x, 0) = H_1\exp(-c_1(x - x_1)^2) - H_2\exp(-c_2(x - x_2)^2). \quad \text{(A30)}$$

The following initial profile can be obtained in the transform space after using the linearized form of the transformation for the spatial variable:

$$\eta(\sigma, 0) \approx H_1\exp(-\frac{1}{256}c_1(\sigma^2 - \sigma_1^2)^2) - H_2\exp(-\frac{1}{256}c_2(\sigma^2 - \sigma_2^2)^2), \quad \text{(A31)}$$
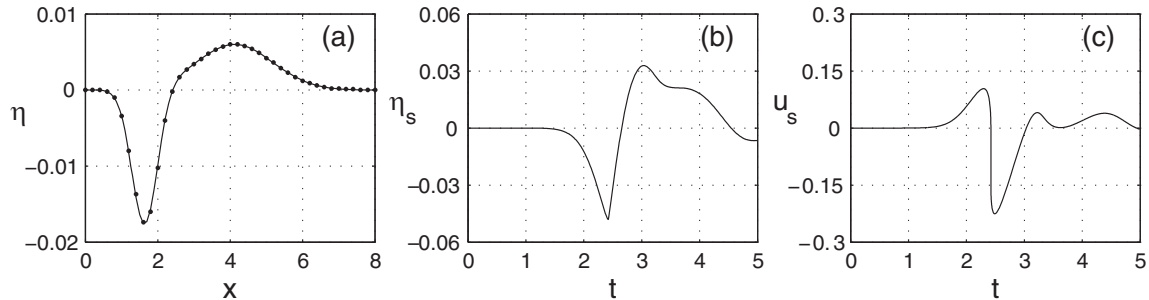
**Figure A6:** (a) The leading-depression initial waveform (A30) presented by Carrier *et al.* (2003) with $H_1$ = 0.006, $c_1$ = 0.4444, $x_1$ = 4.1209, $H_2$ = 0.018, $c_2$ = 4.0, and $x_2$ = 1.6384 (solid line) compared with the one resulting from approximation (evaluated through (A28)) (dots), (b) shoreline wave height, and (c) shoreline velocity.

which leads to the definition of the initial condition $\Phi(\sigma)$:

$$\Phi(\sigma) = -\frac{1}{16}H_1\, c_1\, (\sigma^2 - \sigma_1^2)\, \exp(-\frac{1}{256}c_1(\sigma^2 - \sigma_1^2)^2)$$
$$+\frac{1}{16}H_2\, c_2\, (\sigma^2 - \sigma_2^2)\, \exp(-\frac{1}{256}c_2(\sigma^2 - \sigma_2^2)^2). \quad (A32)$$

Figure A6a compares the initial waveforms defined in the physical space as in (A30) with the one resulting from the approximation of it, i.e., (calculated through (A28)). The linearized form of the spatial variable in the definition of the initial waveforms gives satisfactory comparison. Figures A6b and A6c present the shoreline runup–rundown motion and velocity, respectively, calculated from equation (A29) using the corresponding parts. It should be added that the solution presented here cannot be evaluated when the Jacobian of the transformation, $J = x_\sigma\, t_\lambda - x_\lambda\, t_\sigma$, breaks down. Even though the transformation might become singular at certain points, the solution can still be obtained at other points, since local integration can be performed without prior knowledge of the dependent variables, unlike in numerical methods. This feature is discussed in detail in Synolakis (1987) and Carrier *et al.* (2003), and is not explained further in here.

### 2.2   *Solitary wave on composite beach*

Most topographies of engineering interest can be approximated by piecewise-linear segments allowing the use of LSW to determine approximate analytical results for the wave runup of more complicated waveforms, in closed form. In principle, fairly complex bathymetry can be represented through a combination of positive and/or negative segments and constant-depth segments. Solutions of the LSW (A4) at each segment can be matched analytically at the transition points between the segments, and then the overall amplification factor and reflected waves can be determined, analytically. We consider here an application to check this assertion with a complex topography consisting of three segments and a vertical wall (Fig. A7). Laboratory data
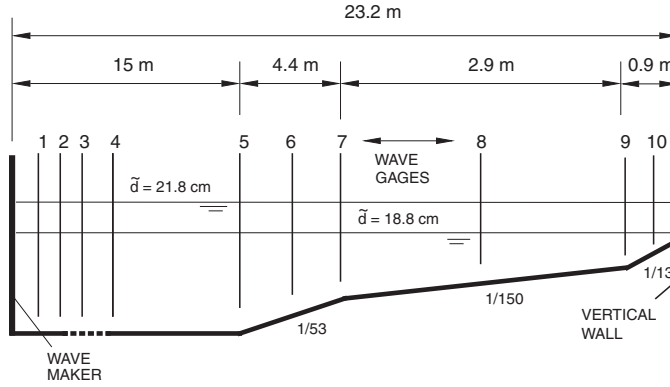
**Figure A7:** Definition sketch for Revere Beach. Not to scale. Transition points and segments are numbered from shoreward to seaward, i.e., segment numbers 1, 2, 3, and 4 show 1/13, 1/150, 1/53, and constant-depth segments, transition points 1, 2, and 3 show transition points between 1/13 and 1/150, 1/150 and 1/53, and 1/53 and constant-depth segment, respectively.

exist for this topography from a U.S. Army Corps of Engineers, Coastal Engineering Research Center, Vicksburg, Mississippi experiment of wave runup on a model of Revere Beach, Massachusetts. This beach profile and the laboratory data are discussed in greater detail in Yeh *et al.* (1996), Kânoğlu (1998), and Kânoğlu and Synolakis (1998). The profile of the model consists of three piecewise-linear slopes of 1:13 (1st segment), 1:150 (2nd segment), and 1:53 (3rd segment) from shoreward to seaward. At the shoreline there is a vertical wall. In the laboratory experiments, to evaluate the overtopping of the seawall, the wavemaker was located 23.22 m and tests were done at two depths, at 18.8 cm and at 21.8 cm.

Kânoğlu (1998) and Kânoğlu and Synolakis (1998) associated constant-depth segment of depth $h_r$ with the matrix:

$$D_{pr} = \left[ \begin{array}{cc} e^{-\frac{i\omega x_p}{\sqrt{h_r}}} & e^{\frac{i\omega x_p}{\sqrt{h_r}}} \\ ie^{-\frac{i\omega x_p}{\sqrt{h_r}}} & -ie^{\frac{i\omega x_p}{\sqrt{h_r}}} \end{array} \right], \tag{A33}$$

and the linearly varying depth region with positive slope $m_r$ is associated with the matrix:

$$Q_{pr} = \left[ \begin{array}{cc} J_0(2\omega\sqrt{h_p}/m_r) & Y_0(2\omega\sqrt{h_p}/m_r) \\ J_1(2\omega\sqrt{h_p}/m_r) & Y_1(2\omega\sqrt{h_p}/m_r) \end{array} \right]. \tag{A34}$$

Above, in equations (A33) and (A34), the first subscript $p$ identifies the transition point, and the second subscript $r$ identifies the segment, i.e., if a segment has two transition points, there are two associated $2 \times 2$ matrices. Here nondimensional quantities are defined as in (A2) using the depth of the 4th segment $\widetilde{h}_4$ as the characteristic length scale.

Using (A33) and (A34), continuities of water surface elevation and its spatial derivative at the transition points lead to the following matrix equa-

tions:

$$Q_{11}V_1 = Q_{12}V_2, \ Q_{22}V_2 = Q_{23}V_3, \ \text{and} \ Q_{33}V_3 = D_{34}V_4, \qquad \text{(A35)}$$

for each transition point. Here column vectors $V_r = [V_{r1}, V_{r2}]^T$ identify unknowns for each segment. One additional condition must be considered at the vertical wall, i.e., perfect reflection. Boundary condition at the wall requires $V_1$ to be a column vector considering perfect reflection, i.e., $Q_w = \left[1, -J_1(2\omega\sqrt{h_w}/m_1)/Y_1(2\omega\sqrt{h_w}/m_1)\right]^T$. $V_1 = Q_w V_{11}$ with $h_w$ is the dimensionless water depth at the wall. Combining (A35) with perfect reflection gives

$$Q_w V_{11} = Q_{11}^{-1} Q_{12} Q_{22}^{-1} Q_{23} Q_{33}^{-1} D_{34} V_4. \qquad \text{(A36)}$$

To evaluate time histories of the surface elevation, the following integral must be evaluated

$$\eta_r(x,t) = \int\limits_{-\infty}^{+\infty} \Phi(\omega)\frac{1}{V_{41}} \left\{ \begin{array}{c} V_{r1}J_0(\frac{2\omega\sqrt{h_r(x)}}{m_r}) + V_{r2}Y_0(\frac{2\omega\sqrt{h_r(x)}}{m_r}) \\ V_{41}e^{-\frac{i\omega x}{\sqrt{h_4}}} + V_{42}e^{\frac{i\omega x}{\sqrt{h_4}}} \end{array} \right\} e^{-i\omega t}d\omega, \qquad \text{(A37)}$$

where $r = 1$, 2, 3 and $V_{41}$ and $V_{42}$ represents incident and reflected wave amplitudes, respectively. The temporal variation of the water surface elevation can be calculated through (A37) evaluating the unknowns in terms of $V_{41}$ through (A36) and (A35).

More interestingly, following analysis of Synolakis (1986) the maximum runup of solitary waves over Revere Beach can be calculated analytically given $\Phi(\omega)$ as in (A9). The amplitude at the shoreline is

$$R(t) = \eta(0,t) = -(4/3)\frac{m_1}{\pi\sqrt{h_w}} \int_{-\infty}^{+\infty} \frac{\text{cosech}(\alpha\omega)e^{i\omega(X_s - X_3 - t)}}{\varphi(\omega) + i\psi(\omega)}d\omega. \qquad \text{(A38)}$$

Here $\varphi(\omega) + i\psi(\omega)$ is a complicated but determinable quite easily from expression (A35) and (A36) in terms of Bessel functions of zero and first order, using symbolic mathematical tools. Kânoğlu (1998) conjectured that $\varphi(z) + i\psi(z)$ is an entire function in the upper half plane, and derived the Laurent series expansion and its asymptotic form as

$$R(t) = 8h_w^{-1/4}H \sum_{n=1}^{+\infty} (-1)^{n+1} n \mathcal{X}^n, \qquad \text{(A39)}$$

where $\mathcal{X} = e^{-\frac{\pi}{\alpha}(X_s - X_3 - t + 2\{\frac{\sqrt{h_1} - \sqrt{h_w}}{m_1} + \frac{\sqrt{h_2} - \sqrt{h_1}}{m_2} + \frac{\sqrt{h_3} - \sqrt{h_2}}{m_3}\})}$. This is a power series of the form $\sum(-1)^{n+1}n\mathcal{X}^n$ and its maximum is equal to 1/4. Therefore the maximum runup for solitary waves propagating up Revere Beach is given by the runup law,

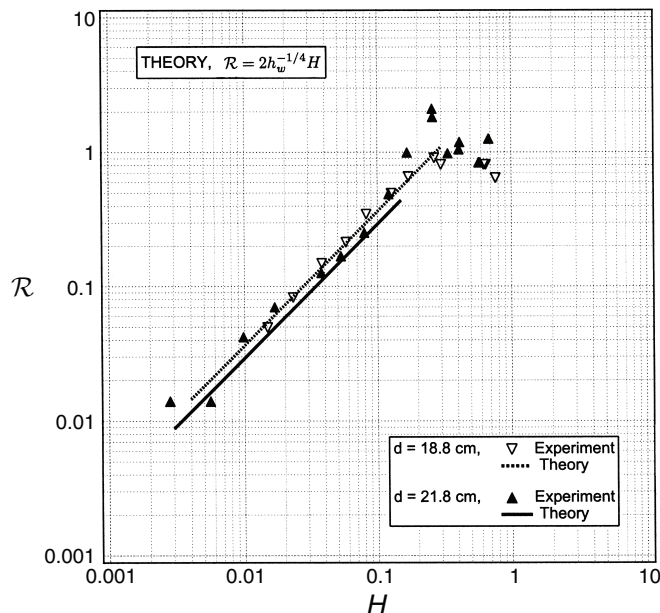$$\mathcal{R} = 2h_w^{-1/4}H. \qquad \text{(A40)}$$

**Figure A8:** Comparison of maximum runup values for the linear analytical solution (A39) and laboratory results for two different depths, i.e., $\widetilde{d} = 18.8$ cm and $\widetilde{d} = 21.8$ cm.

The runup law above suggests that the maximum runup only depends on the depth at the seawall fronting the beach, and it does not depend on any of the three slopes in front of the seawall. The runup law (A40) predicts the nonbreaking data surprisingly well (Fig. A8).

Note that no Jacobian regularization conditions as yet exist for wave evolution on composite beaches, and this theory can only be applied with caution. For lack of a better method, it is recommended that a limiting height be determined for applying this methodology on a composite beach, by finding the limiting height for the single beach with slope equal to the least steep slope in the composite topography under consideration. This practice will produce adequate validity thresholds for bathymetries such as Revere Beach, but it should not be used when abrupt changes in bathymetry exist. In most cases, for the range of wave-steepness and beach slopes relevant in tsunami studies, this method will give good results with fairly small computational effort.

### 2.3 Subaerial landslide on simple beach

Liu *et al.* (2003) considered tsunami generation by a moving slide on a uniformly sloping beach, using the forced linear shallow water-wave equation as in Tuck and Hwang (1972);

$$\frac{\partial^2 \eta}{\partial t^2} - \frac{tan\beta}{\mu} \frac{\partial}{\partial x}\left(x \frac{\partial \eta}{\partial x}\right) = \frac{\partial^2 h_0}{\partial t^2}, \tag{A41}$$

in the dimensionless form. Here $z = \eta(x,t)$ is the free surface elevation and $z = -h(x,t)$ the sea floor. On a sloping beach $h(x,t) = H(x) - h_0(x,t)$ with $H(x) = x \tan\beta/\mu$; $\tan\beta$ is the beach slope, $h_0(x,t)$ is the time-dependent perturbation of the sea floor with respect to the uniformly sloping beach, $\widetilde{\delta}$ and $\widetilde{L}$ are the maximum vertical thickness of the sliding mass and its horizontal length, respectively, and $\mu = \widetilde{\delta}/\widetilde{L}$. Normalization is done as

$$(\eta, h, H, h_0) = \frac{(\widetilde{\eta}, \widetilde{h}, \widetilde{H}, \widetilde{h}_0)}{\widetilde{\delta}}, \quad x = \frac{\widetilde{x}}{\widetilde{L}}, \text{ and } t = \frac{\widetilde{t}}{\sqrt{\widetilde{\delta}/\widetilde{g}}/\mu}. \tag{A42}$$

Here again quantities with tilde represent dimensional quantities. The focus is on thin slides where $\mu = \widetilde{\delta}/\widetilde{L} \ll 1$. Since the shallow water-wave assumption requires that $\tan\beta \ll 1$, then $\tan\beta/\mu \sim O(1)$.

Consider a translating Gaussian shaped mass, initially at the shoreline as in Liu *et al.* (2003), i.e., the seafloor can be described by $h_0(x,t) = \exp\left[-(\xi - t)^2\right]$ with $\xi = 2\sqrt{\mu x/\tan\beta}$. Once in motion, the mass moves at constant acceleration. Solution of (A41) under this translating Gaussian shape is given as

$$\eta(\xi, t) = \int_0^\infty J_0(\rho\xi)\rho\left[a(\rho)\cos(\rho t) + \frac{1}{\rho}b(\rho)\sin(\rho t)\right] d\rho + \frac{1}{3}(h_0 - \xi\frac{\partial h_0}{\partial\xi}), \tag{A43}$$

in Liu *et al.* (2003) with

$$a(\rho) = \int_0^\infty \varsigma J_0(\rho\varsigma)\left[-\frac{1}{3}(h_0 - \xi\frac{\partial h_0}{\partial\xi})\right]\Big|_{t=0,\ \xi\to\varsigma} d\varsigma, \tag{A44}$$

$$b(\rho) = \int_0^\infty \varsigma J_0(\rho\varsigma)\left[\frac{1}{3}(2\frac{\partial h_0}{\partial t} + \varsigma\frac{\partial^2 h_0}{\partial\xi\partial t})\right]\Big|_{t=0,\ \xi\to\varsigma} d\varsigma. \tag{A45}$$

Two specific examples are presented in Figs. A9 and A10. Maximum runup estimates, maximum wave height at $x = 0$, from the analytical solution (A43) and the numerical solution of Liu *et al.* (2003) are given in Fig. A11.

## 3 Laboratory benchmarking

As a preamble, and before describing the benchmark laboratory tests, waves are generated in the laboratory by moving vertical paddles. While other generation methods exist, hydraulic paddles allow for the precise and repeatable specification of arbitrary trajectories. In one-dimensional wave channels—also known as wave flumes and sometimes wave tanks—there is usually only one paddle, perpendicular to the water surface. As the paddle displaces horizontally, free-surface waves are generated. In two dimensional wave basins, there are often multiple paddles that can move horizontally. The experiments to be described were conducted in wave basins with multiple paddles. This kind of generator is known as the snake generator. When the paddles move independently, its motion resembles the ophite motion of a snake.
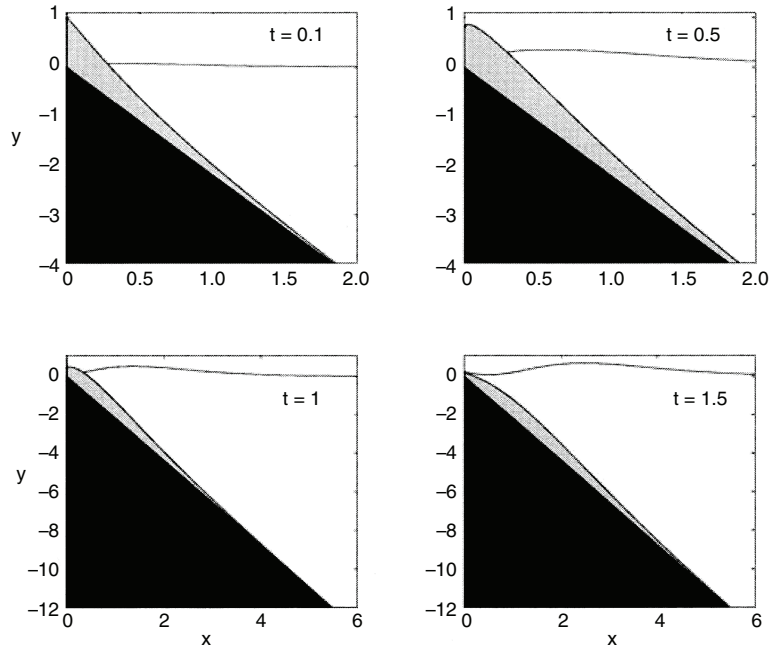
**Figure A9:** Spatial snapshots of the analytical solution at four different times for a beach slope, $\beta = 5°$, and landslide aspect ratio, $\mu = 0.05$ ($\tan \beta / \mu = 1.75$). The slide mass is indicated by the light shaded area, the solid beach slope by the black region, and $\eta$ by the solid line (Liu *et al.*, 2003).
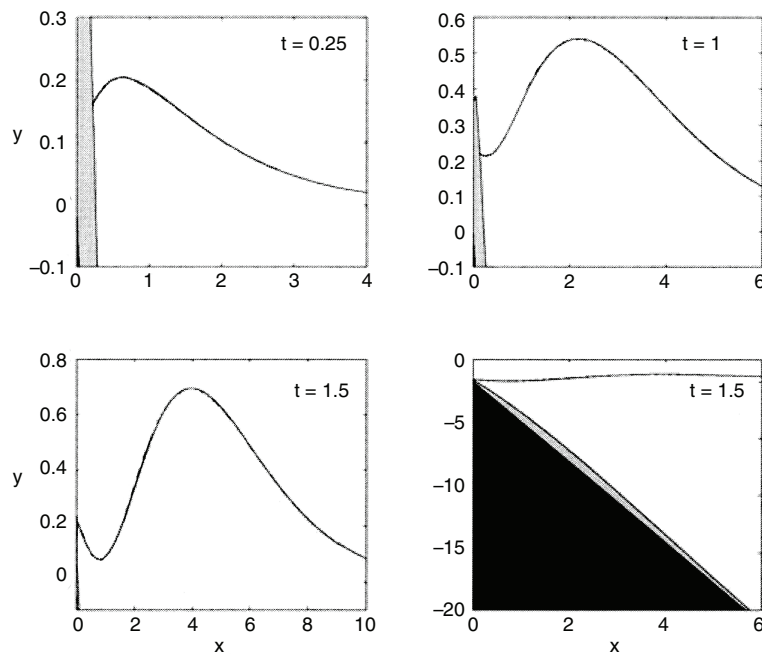


**Figure A10:** Spatial snapshots of the analytical solution at three different times for a beach slope, $\beta = 10°$, and $\mu = 0.05$ ($\tan \beta / \mu = 3.5$). The slide mass is indicated by the light shaded area, and the solid beach slope by the black region. In the lower right panel, the water depth and landslide profile is shown at $t = 1.5$, the same time as shown in the lower left plot (Liu *et al.*, 2003).
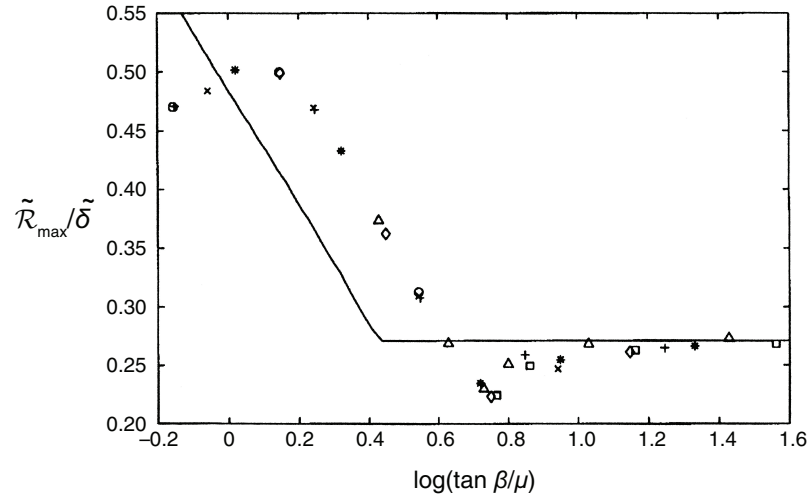
**Figure A11:** Maximum runup as a function of $\log(\tan\beta/\mu)$. The analytical solutions are shown by the solid line, and the various symbols are from NLSW simulations of Liu *et al.* (2003), corresponding to different slopes ranging from $2°$ to $20°$.

They are also known as Directional Wave Spectrum Generators (DWSGs). In the U.S., such DWSGs exist at the Coastal and Engineering Laboratory of the U.S. Army Corps of Engineers in Vicksburg, Mississippi, at the Texas A&M University in College Station, Texas, and at Oregon State University in Corvallis, Oregon.

Here five sets of experiments will be described in detail for laboratory benchmarking data: solitary wave experiments on a 1:20 sloping beach (Synolakis, 1987), solitary wave runup over a composite beach (Kânoğlu, 1998; Kânoğlu and Synolakis, 1998), conical island experiments (Liu *et al.,* 1995; Kânoğlu, 1998; Kânoğlu and Synolakis, 1998), and tsunami runup onto a complex three-dimensional beach (Takahashi, 1996), and tsunami generation and runup due to three-dimensional landslide (Liu *et al.,* 2005).

### 3.1   Solitary wave on a simple beach

In this set of experiments, the 31.73 m-long, 60.96 cm-deep, and 39.97 cm-wide California Institute of Technology, Pasadena, California wave tank was used with water at varying depths. The tank is described by Hammack (1972), Goring (1978), and Synolakis (1986, 1987). The bottom of the tank consisted of painted stainless steel plates. Carriage rails run along the whole length of the tank, permitting the arbitrary movement of instrument carriages. A ramp was installed at one end of the tank to model the bathymetry of the canonical problem of a constant-depth region adjoining a sloping beach. The ramp had a slope of 1:19.85. The ramp was sealed to the tank side walls. The toe of the ramp was distant 14.95 m from the rest position of the piston generator used to generate waves.

A total of more than 40 experiments with solitary waves running up the sloping beach were performed, with wave depths ranging from 6.25 cm to 38.32 cm. Solitary waves are uniquely defined by their maximum height $\widetilde{H}$ to depth $\widetilde{d}$ ratio and the depth, i.e., $\widetilde{H}/\widetilde{d}$ and $\widetilde{d}$ are sufficient to specify the wave. $\widetilde{H}/\widetilde{d}$ ranged from 0.021 to 0.626. Breaking occurs when $\widetilde{H}/\widetilde{d} > 0.045$, for this particular beach. This is the same set of experiments used to validate the maximum runup analytical predictions presented in section A2.1.1.

Initial location, $X_s$ in the analytical consideration (A8), changes with different wave heights. The reason $X_s$ distance varies is that solitary waves of different heights have different effective "wavelengths." A measure of the "wavelength" of a solitary wave is the distance between the point $x_f$ on the front and the tail $x_t$ where the local height is 1% of the maximum, i.e., $\eta(x_f, t = 0) = \eta(x_t, t = 0) = (\widetilde{H}/\widetilde{d})/100$. The distance $X_s$ is at an offshore location where only 5% of the solitary wave is already over the beach, so that scaling can work. Therefore, in the laboratory experiments initial wave heights are identified at a point $X_s = X_0 + (L/2)$ where $L/2 = (1/\gamma)\operatorname{arccosh}\sqrt{20}$ with $\gamma = \sqrt{3(\widetilde{H}/\widetilde{d})/4}$. In the laboratory, even solitary waves can dissipate. If the wave height is measured far offshore and used as an initial condition for non-dissipative numerical models, the comparisons will be less meaningful, as the solitary wave will slightly change as it propagates in the laboratory. By keeping the same relative offshore distance for defining the initial condition, meaningful comparisons are assured.

While only 10 wave gages were used in each experimental run, the generation was extremely repeatable. As experiments were repeated for each wave height, the wave gages were moved to different locations, and the same $\widetilde{H}/\widetilde{d}$ wave was generated again until a sufficient number of data points existed to resolve the entire wave profile. In Synolakis (1987) two different comparisons are presented: one is the amplitude variation at specific $x$-locations, and the second is the amplitude variation at specific $t$-times, the latter resembling the image that a photograph from the side with a large depth of field and angular range would show.

This set of laboratory data has been used extensively for code validation: refer to Synolakis (1987), Zelt (1991), Titov and Synolakis (1995, 1997, 1998), Titov and González (1997), Grilli *et al.* (1997), Li and Raichlen (2000, 2001, 2002). In particular, the data sets for the $\widetilde{H}/\widetilde{d} = 0.0185$ (Fig. A4) nonbreaking and $\widetilde{H}/\widetilde{d} = 0.3$ (Fig. A12) breaking solitary waves seem the most often used and most appropriate for code validation.

## 3.2   *Solitary wave on a composite beach*

Revere Beach is located approximately 6 miles northeast of Boston in the City of Revere, Massachusetts. To address beach erosion and severe flooding problems, a physical model of the beach was constructed at the Coastal Engineering Laboratory of the U.S. Army Corps of Engineers, Vicksburg, Mississippi facility, earlier known as Coastal Engineering Research Center.

The model consists of three piecewise-linear slopes of 1:53, 1:150, and 1:13 from seaward to shoreward. At the shoreline there is a vertical wall (Fig. A7). In the laboratory, to evaluate the overtopping of the seawall,
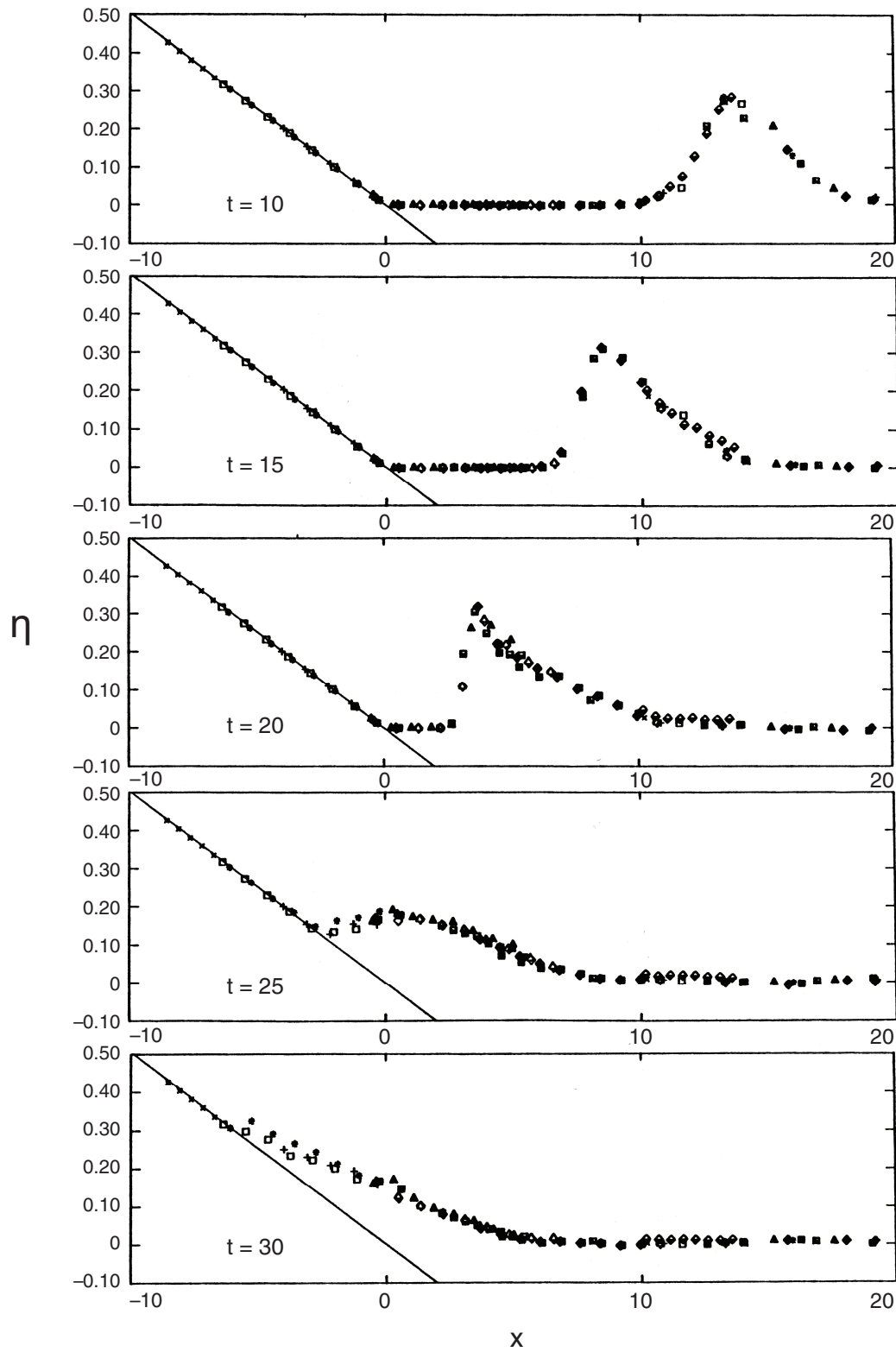
**Figure A12:** Time evolution of $H = 0.3$ initial wave over a sloping beach with $\cot \beta = 19.85$ from $t = 10$ to 30 with 5 increments. Constant-depth segment starts at $X_0 = 19.85$. Markers show a different realization of experimental results of Synolakis (1987).

the wavemaker was located at 23.22 m and tests were done at two depths, at 18.8 cm and at 21.8 cm. Water surface elevations were measured with 10 wave gages, and LDV measurements were performed at two different locations. The maximum runup on the vertical wall was measured visually.

In the experiments, solitary waves of different heights were generated, and the runup variation for solitary waves striking a vertical wall was determined experimentally. The results were used as benchmark data to validate 1+1 numerical codes in the 1995 Friday Harbor, Seattle, Washington workshop, as discussed in Yeh *et al.* (1996), and by Kânoğlu (1998) and Kânoğlu and Synolakis (1998) in validating their analytical formulation.

In terms of specific measurements, time histories of the water surface elevations exist for $\widetilde{H}/\widetilde{d} = 0.038$ at $\widetilde{x} = 12.22$ m, $\widetilde{H}/\widetilde{d} = 0.259$ at $\widetilde{x} = 13.96$ m, and for $\widetilde{H}/\widetilde{d} = 0.681$ at $\widetilde{x} = 14.37$ m. These are the locations where the solitary waves of the given $\widetilde{H}/\widetilde{d}$ are centered for the same reason explained for the solitary wave experiments over a 1:19.85 beach. In all cases, $\widetilde{d} = 21.8$ cm. $\widetilde{x} = 0$ is at one end of the wave flume, i.e., the initial shoreline where the vertical wall is at $\widetilde{x} = 23.22$ m. Other water-surface elevation time series were measured midway in each sloping segment, i.e., at $\widetilde{x} = 17.22$ m and $\widetilde{d} = 17.7$ cm, at $\widetilde{x} = 20.86$ m and $\widetilde{d} = 12.5$ cm and $\widetilde{x} = 22.80$ m and $\widetilde{d} = 8.1$ cm. Time histories of water surface elevations are given in Figs. A13, A14, and A15 for three different wave heights. The measured maximum runup values are given in Table A1 for the three cases presented here. Maximum runup measurements for the whole experiments are presented in Fig. A8.

**Table A1:** Maximum runup measurements on the laboratory model of Revere Beach.

| $\widetilde{H}/\widetilde{d}$ | $\widetilde{\mathcal{R}}$ | $\widetilde{\mathcal{R}}/\widetilde{d}$ |
|---|---|---|
| 0.038 | 2.7 cm | 0.13 |
| 0.259 | 45.7 cm | 2.10 |
| 0.681 | 27.4 cm | 1.26 |

When modeling these experiments, care is needed in calculations in the near-wall region. As the depth goes to zero, the wave breaks closer to the shoreline. The breaking wave collapses on the wall, and the air void explodes producing a splash which cannot be modeled effectively, except with very high resolution codes.

### 3.3   Solitary wave on a conical island

Motivated by the catastrophe in Babi Island, Indonesia (Yeh *et al.*, 1994), during the 1992 Flores Island tsunami, large-scale laboratory experiments were performed at Coastal Engineering Research Center, Vicksburg, Mississippi, in a 30 m-wide, 25 m-long, and 60 cm-deep wave basin (Fig. A16). Waves were realistically created in the tank by a horizontal wave generator with 60 different paddles each 46 cm-wide and moving independently. These experiments provided runup observations for validating numerical models and supplemented comparisons with analytical results (Kânoğlu and Synolakis, 1998).
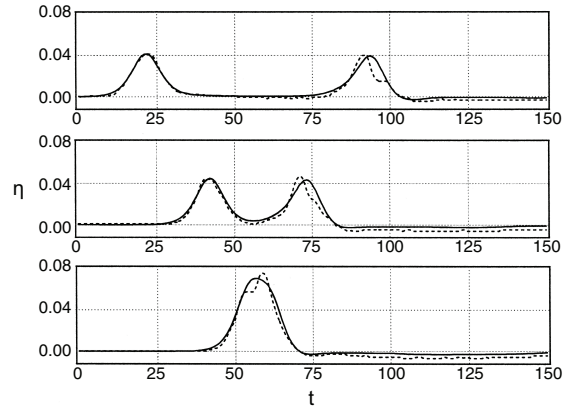
**Figure A13:** Comparison of the time histories of the free surface elevations midway in each sloping segment for the analytical solution of Kânoğlu and Synolakis (1998) and the laboratory data for $\tilde{H}/\tilde{d} = 0.038$ solitary wave.
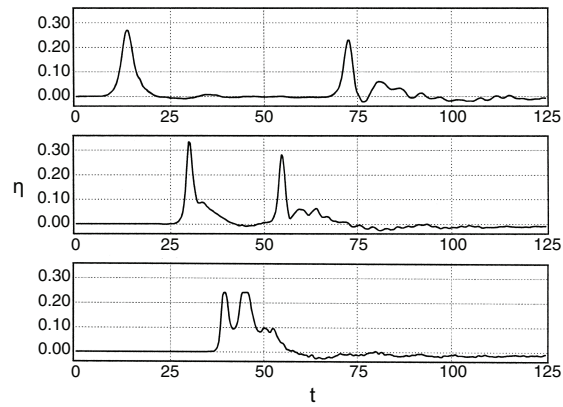


**Figure A14:** The laboratory data for the time histories of the free surface elevations midway in each sloping segment for $\tilde{H}/\tilde{d} = 0.259$ solitary wave.
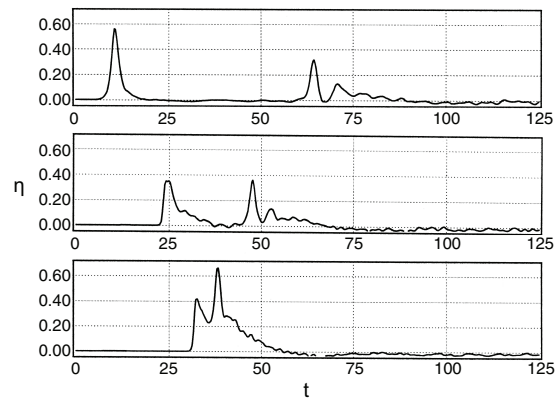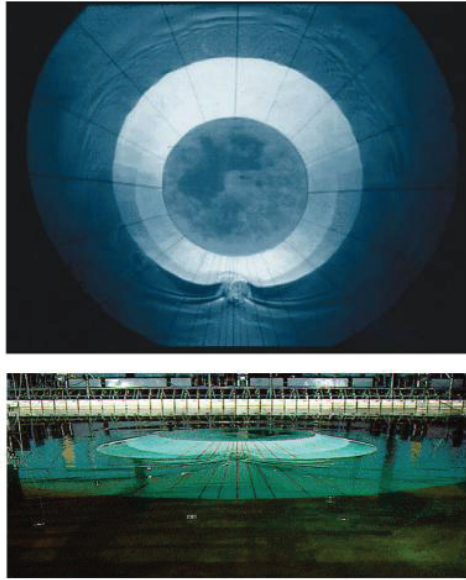


**Figure A15:** The laboratory data for the time histories of the free surface elevations midway in each sloping segment for $\tilde{H}/\tilde{d} = 0.681$ solitary wave.

**Figure A16:** View of conical island (top) and basin (bottom).

The detailed experiments are described elsewhere in greater detail (Liu *et al.,* 1995; Briggs *et al.,* 1995; Kânoğlu, 1998; Kânoğlu and Synolakis, 1998). Briefly, a Directional Spectral Wave Generator (DSWG), located at $\widetilde{x} = 12.96$ m from the island, generated waves with an initial solitary wave-like profile. The 27.42 m-long DSWG consists of sixty 46 cm-wide and 76 cm-high individual paddles, each of which can be driven independently. This allowed performance of experiments with different wave crest lengths. However, the cases presented here were performed using all the paddles. Experimental results for different wave crest lengths are given in Briggs *et al.* (1995) and Kânoğlu (1998).

In the physical model, a 62.5 cm-high, 7.2 m toe-diameter, and 2.2 m crest-diameter circular island with a 1:4 slope was located in the basin (Fig. A17). Experiments were conducted at two different water depths, 32 cm and 42 cm, but presented here with dimensionless solitary wave heights $\widetilde{H}/\widetilde{d}$ equal to 0.045, 0.091, and 0.181 at 32 cm. Each experiment was repeated at least twice and maximum runup heights around the perimeter of the island were measured at 24 locations. Wavemaker signals were presented in Fig. A19 for these cases to allow direct implementation of these solitary waves as a wavemaker motion in the numerical models. Water-surface time histories were measured with 27 wave gages located around the perimeter of the island (Fig. A18). However, here, time histories of the surface elevation around the circular island are given at four locations, i.e., in the front of the island at the toe and gages closest to the shoreline with the numbers 9, 16, and 22 located at the $0°$, $90°$, and $180°$ radial lines, respectively (Figs. 20 and 21).

These experiments were used as benchmark tests for validating 2+1 nu-
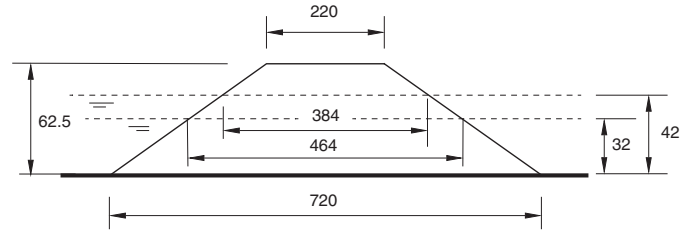
**Figure A17:** Definition sketch for conical island. All dimensions are in cm. Not to scale.
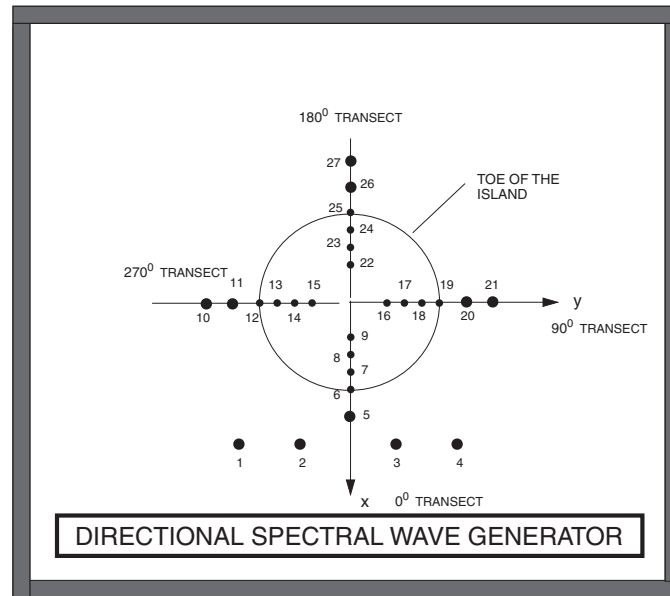


**Figure A18:** Schematic showing gage locations around the conical island. Not to scale.
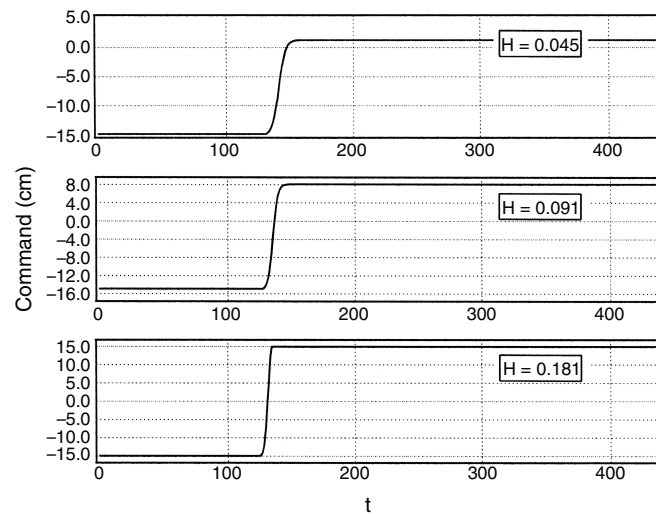


**Figure A19:** Wavemaker motions for the generation of $\tilde{H}/\tilde{d} = 0.045$, 0.091, and 0.181 solitary waves. Target wave heights are given in the insets.
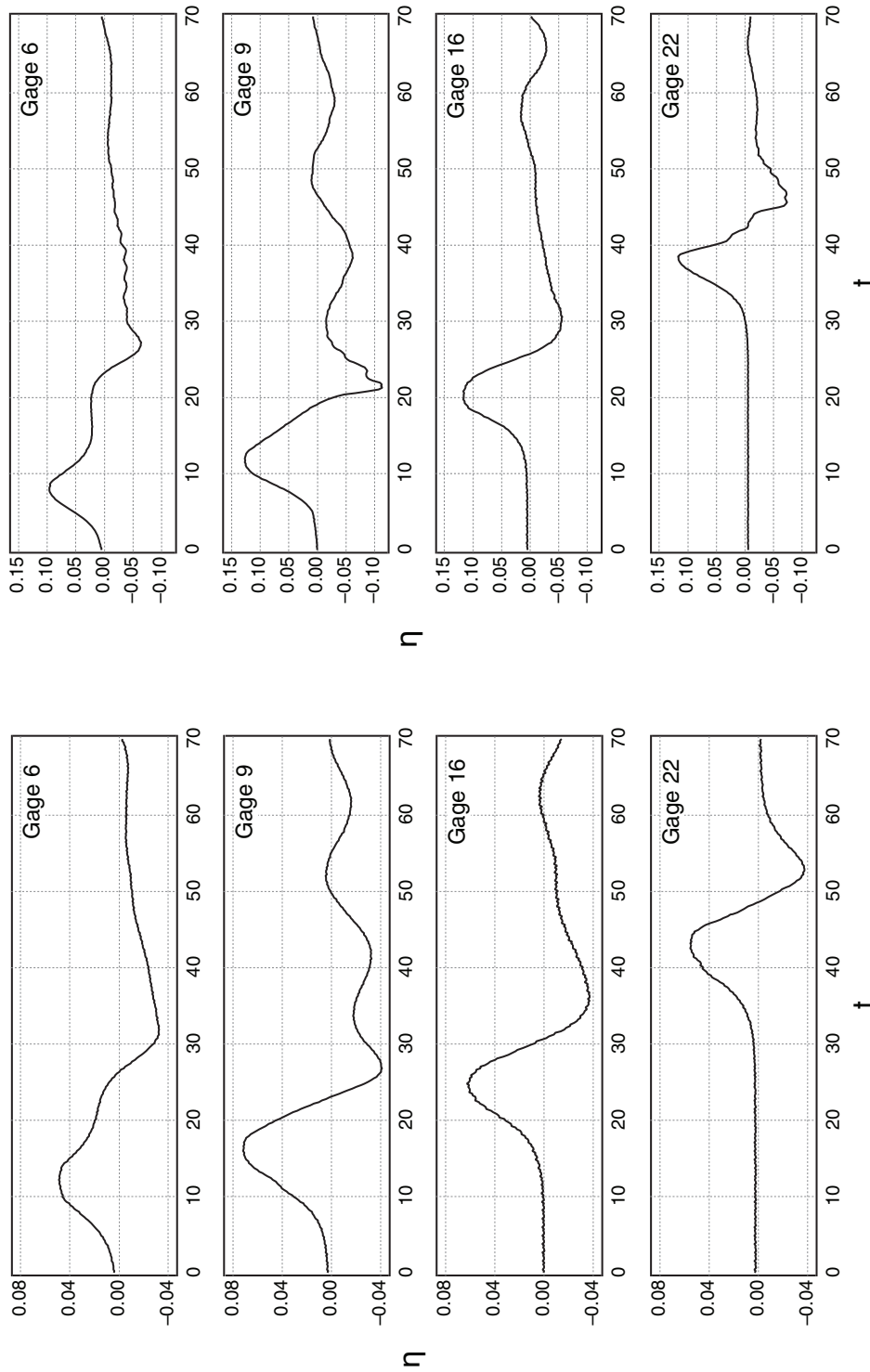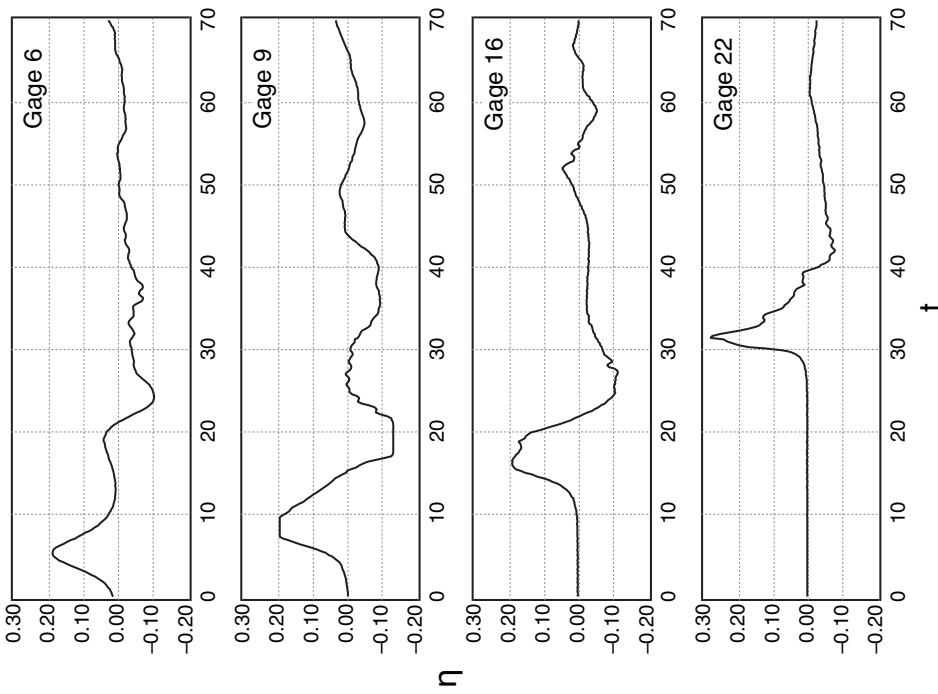
**Figure A20:** Laboratory data for the time histories of surface elevation for a $\tilde{H}/\tilde{d} = 0.045$ solitary wave at four gages and $\tilde{d} = 32$ cm. Gage 6 is located at the toe of the conical island on 0° radial line. Gages 9, 16, and 22 are the gages closest to the shoreline on the 0°, 90°, and 180° radial lines, respectively. Initial wave is defined half-wavelength (L/2, i.e., gages 1 to 4) away from the toe of the conical island.

**Figure A21:** Laboratory data for the time histories of surface elevation for a $\tilde{H}/\tilde{d} = 0.091$ solitary wave at four gages and $\tilde{d} = 32$ cm. Gage 6 is located at the toe of the conical island on 0° radial line. Gages 9, 16, and 22 are the gages closest to the shoreline on the 0°, 90°, and 180° radial lines, respectively. Initial wave is defined half-wavelength (L/2, i.e., gages 1 to 4) away from the toe of the conical island.

**Figure A23:** Maximum runup heights from the laboratory data for three solitary waves $\tilde{H}/\tilde{d} = 0.045$, $0.091$, and $0.181$ and $\tilde{d} = 32$ cm. Initial waves are defined half-wavelength (L/2, i.e., gages 1 to 4) away from the toe of the conical island.



**Figure A22:** Laboratory data for the time histories of surface elevation for a $\tilde{H}/\tilde{d} = 0.181$ solitary wave at four gages and $\tilde{d} = 32$ cm. Gage 6 is located at the toe of the conical island on 0° radial line. Gages 9, 16, and 22 are the gages closest to the shoreline on the 0°, 90°, and 180° radial lines, respectively. Initial wave is defined half-wavelength (L/2, i.e., gages 1 to 4) away from the toe of the conical island.
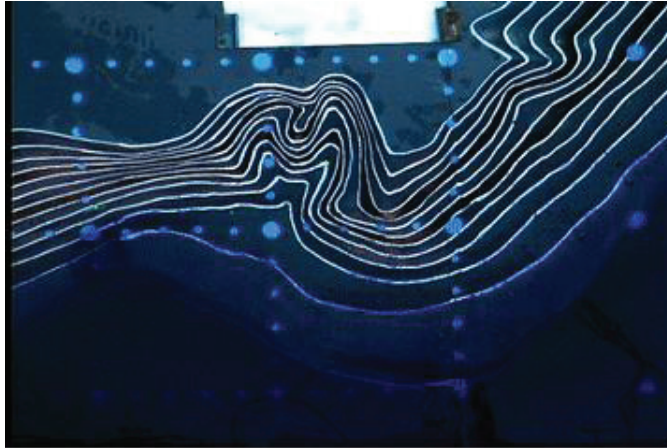
**Figure A24:** Bathymetric profile for experimental setup for Monai Valley experiment.

merical codes in the 1995 Friday Harbor, Seattle, Washington Long-Wave Runup Models Workshop (Yeh *et al.,* 1996).

### 3.4 Tsunami runup onto a complex three-dimensional beach; Monai Valley

The Hokkaido-Nansei-Oki tsunami of 1993 that struck Okushiri Island, Japan, with extreme runup height of 30 m and currents of the order of 10–18 m/sec was a disaster, but provided fortuitous high-quality data. The extreme tsunami runup mark was discovered at the tip of a very narrow gulley within a small cove at Monai. High resolution seafloor bathymetry existed before the event and when coupled with bathymetric surveys following the event allowed meaningful identification of the seafloor deformation.

A 1/400 laboratory model of Monai was constructed in a 205 m-long, 6 m-deep, and 3.5 m-wide tank at Central Research Institute for Electric Power Industry (CRIEPI) in Abiko, Japan and partly shown in Fig. A24. The laboratory setup closely resembles the actual bathymetry. The incident wave from offshore, at the water depth $\widetilde{d} = 13.5$ cm is known. There are reflective vertical sidewalls at $\widetilde{y} = 0$ and 3.5 m (Fig. A25). The entire computational area is 5.448 m × 3.402 m, and the recommended time step and grid sizes for numerical simulations are $\widetilde{\Delta x} = \widetilde{\Delta y} = 1.4$ cm and $\widetilde{\Delta t} = 0.05$ sec.

The input wave is a LDN with a leading-depression height of −2.5 mm with a crest of 1.6 cm behind it (Fig. A26). Waves were measured at thirteen locations and complete time histories are given at three locations, i.e., $(\widetilde{x}, \widetilde{y}) = (4.521, 1.196)$, $(4.521, 1.696)$, and $(4.521, 2.196)$ in meters (Fig. A27). These experiments were used in the 2004 Catalina Island, Los Angeles, California NSF Long-Wave Runup Models Workshop.
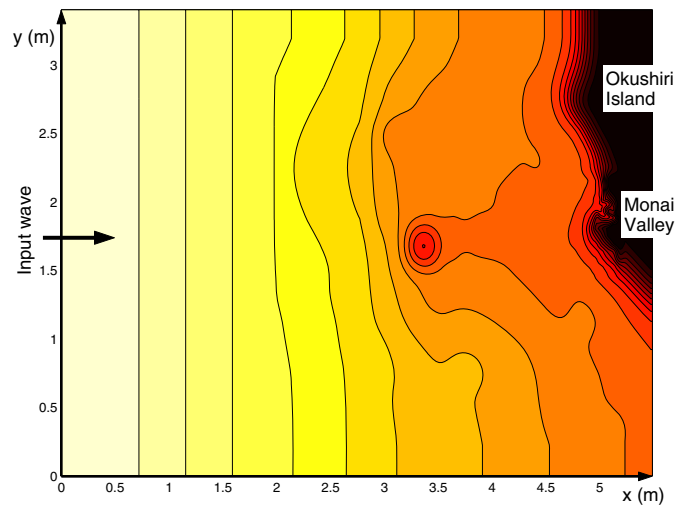
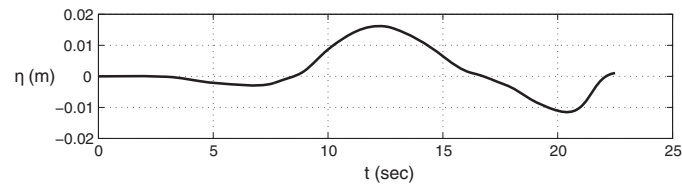**Figure A25:** Computational area for Monai Valley experiment.



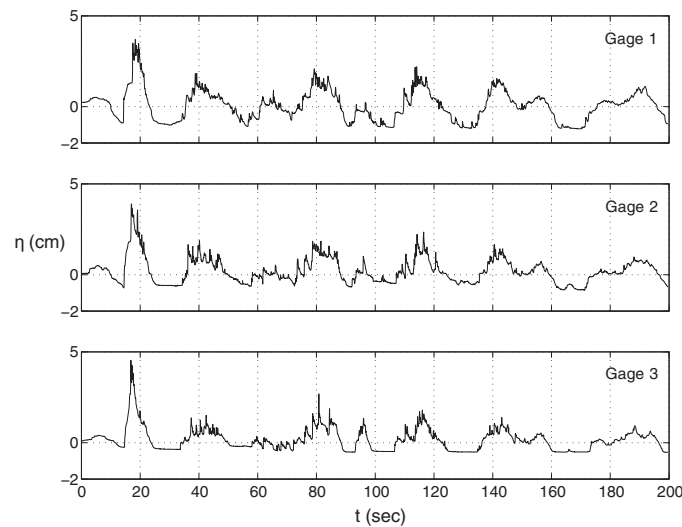**Figure A26:** Initial wave profile for Monai Valley experiment.



**Figure A27:** Time series of surface elevation at three different gages. Gages 1, 2, and 3 are located at (4.521, 1.196), (4.521, 1.696), and (4.521, 2.196) meters, respectively.
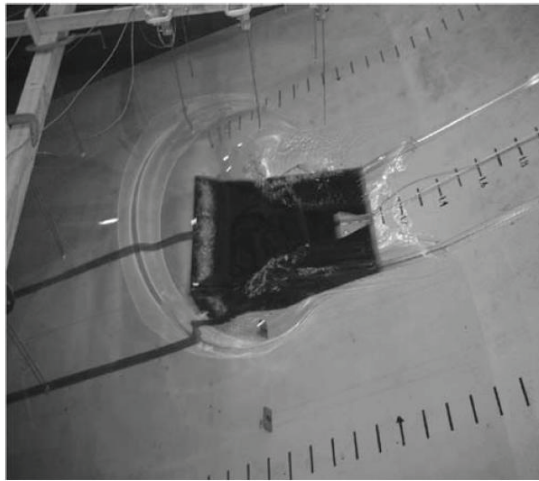
**Figure A28:** Picture of part of the experimental setup.

### 3.5 Tsunami generation and runup due to three-dimensional landslide

As discussed, landslide wave generation remains the frontier in terms of numerical modeling, particularly for aerial slides. These involve not only the rapid change of the seafloor, but also the impact of the slide on the shoreline. Details and more experimental results can be found in Liu *et al.* (2005).

Large-scale experiments have been conducted in a wave tank with a 104 m-long, 3.7 m-wide, and 4.6 m-deep wave channel with a plane slope (1:2) located at one end of the tank; part of the experimental setup is shown in Fig. A28. A solid wedge was used to model the landslide. The triangular face had a horizontal length of $b = 91$ cm, a vertical face with a height of $a = 45.5$ cm, and a width of $w = 61$ cm (Fig. A29). The horizontal surface of the wedge was initially positioned either a small distance above or below the still water level to reproduce a subaerial or submarine landslide. The block was released from rest, abruptly moving downslope under gravity, rolling on specially designed wheels (with low friction bearings) riding on aluminum strips with shallow grooves inset into the slope. The wedge was instrumented with an accelerometer to accurately define the acceleration-time history and a position indicator to independently determine the velocity and position time histories. Wedge positions are given in Fig. A30 for the two cases presented here.

A sufficient number of wave gages were used to determine the seaward propagating waves, the waves propagating to either side of the wedge, and for the submerged case, the water surface-time history over the wedge. In addition, the time history of the runup on the slope was accurately measured. Time histories of the surface elevations and runup measurements for two cases are presented in Figs. A31 and A32 for the submerged cases with

**Table A2:** Fault parameters of DCRC-17a.

| Subfault | North | Central | South |
|---|---|---|---|
| Width (km) | 25 | 25 | 25 |
| Length (km) | 90 | 30 | 24.5 |
| Strike (deg) | 188 | 175 | 163 |
| Dip angle (deg) | 35 | 60 | 60 |
| Slip angle (deg) | 80 | 105 | 105 |
| Depth (km) | 10 | 5 | 5 |
| Dislocation (m) | 5.71 | 2.50 | 12.00 |
| Origin ($°$) | 139.40°E 41.13°N | 139.25°E 42.34°N | 139.30°E 42.10°N |
| $M_0$ ($\times 10^{27}$ dyn cm) | 3.85 | 0.56 | 2.21 |

$\Delta = -0.025$ m and $\Delta = -0.1$ m, respectively. While a total of more than 50 experiments with moving wedges, hemispheres, and rectangles were conducted, the wedge experiments were used as benchmark tests in the 2004 Catalina Island, Los Angeles, California workshop.

## 4   Field benchmarking

Verification of a model in a real-world setting is an important part of an operational model validation. No analytical or laboratory data comparisons (or any limited number of tests, for that matter) can assure robust model performance in the operational environment. Test comparisons with real-world data provide an additional important step in the validation of a model to perform well during operational implementation.

### 4.1   *Okushiri Island*

Okushiri Island, Japan, data was the benchmark problem for the 2nd International Long-Wave Runup Models Workshop, Friday Harbor, Washington (Takahashi, 1996). The magnitude $M_s = 7.8$ Hokkaido Nansei-Oki, Japan, earthquake occurred on 12 July 1993 with the hypocenter located at 37 km depth at 42.76°N and 139.32°E off the southwestern coast of Hokkaido, Japan. The Disaster Control Research Center (DCRC), Japan, digitized the bathymetric and topographic data from several sources (Fig. A33).

DCRC constructed initial wave profile DCRC-17a with 4.9 m and 2.2 m uplift and 1.1 m subsidence (depression) as shown in Fig. A34 and given in Table A2. There are several observations which need to be explained by numerical modeling:

- Arrival of the first wave to Aonae 5 min after the earthquake should be estimated with the numerical model. Also, a numerical model should reveal two waves at Aonae approximately 10 min apart; while the first wave came from the west, the second wave came from the east. In addition, two tide gage records at Iwanai and Esashi given in Fig. A35 need to be estimated.

- Maximum runup distribution around Okushiri Island should compare well with the field measurements (Fig. A36). High runup height at
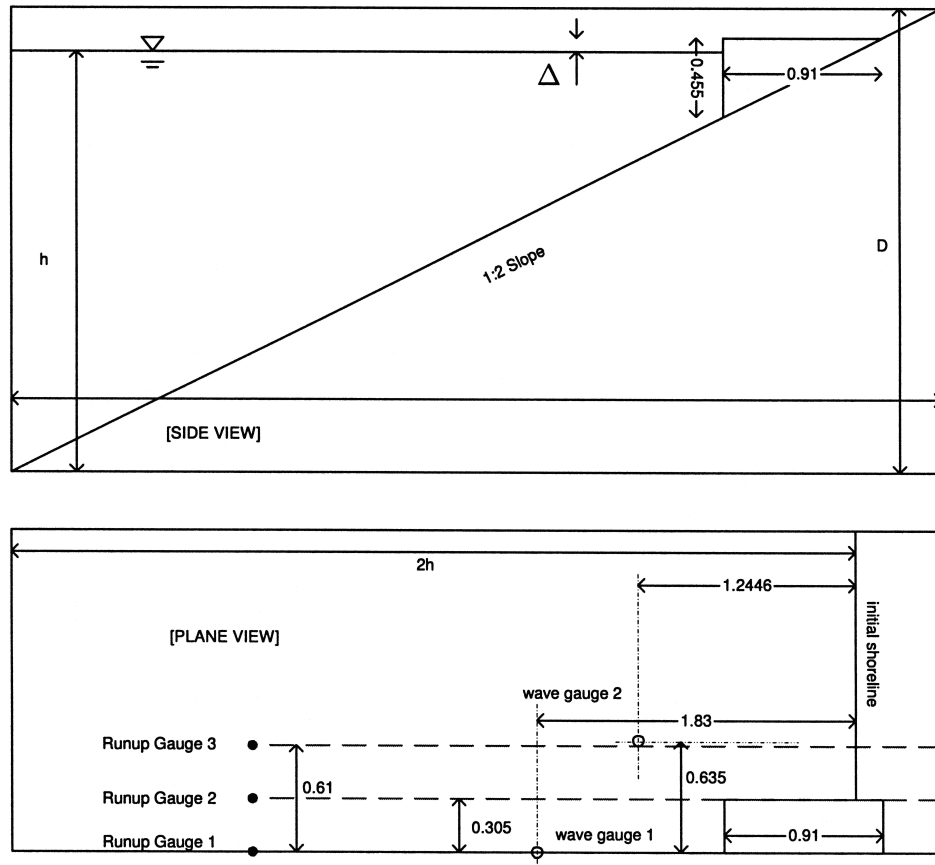
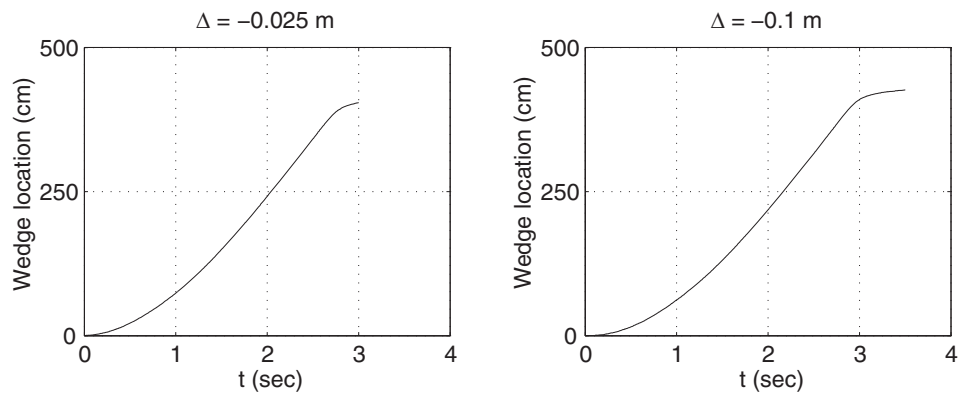**Figure A29:** Schematic of the experimental setup.



**Figure A30:** Time histories of the block motion for the submerged case with $\Delta = -0.025$ m and $-0.1$ m.
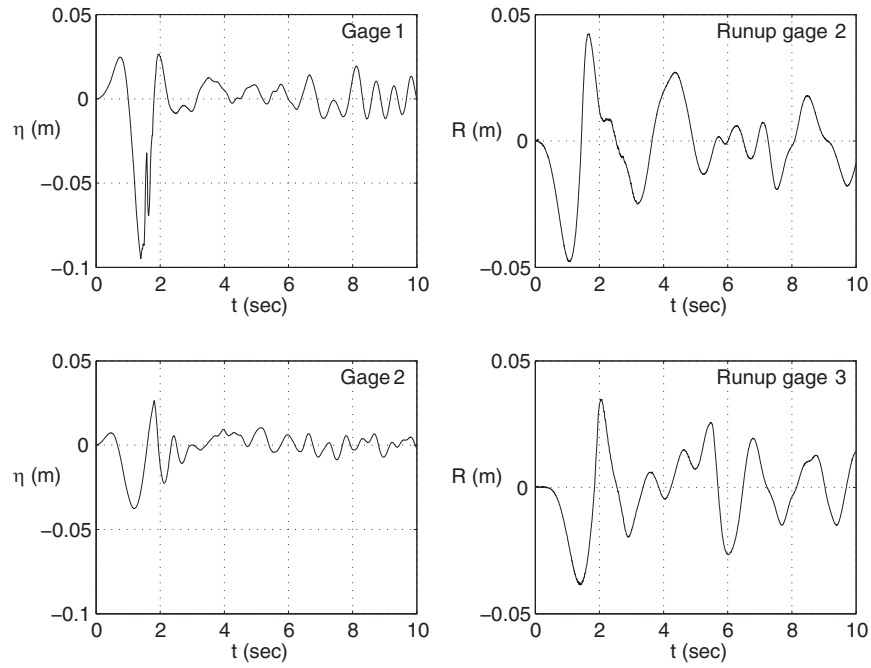
**Figure A31:** Time histories of the surface elevation and runup measurements for the submerged case with $\Delta = -0.025$ m.
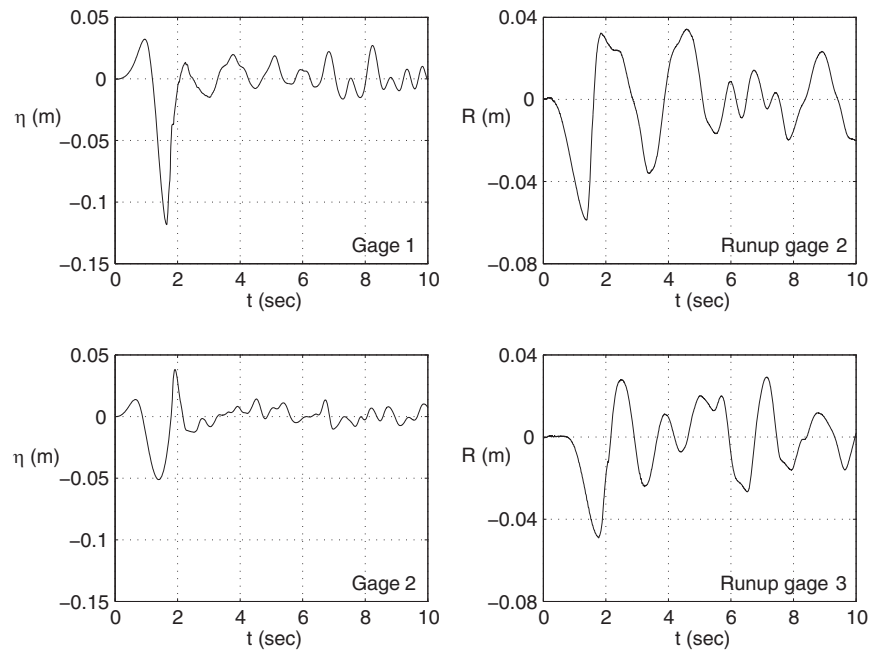


**Figure A32:** Time histories of the surface elevation and runup measurements for the submerged case with $\Delta = -0.1$ m.
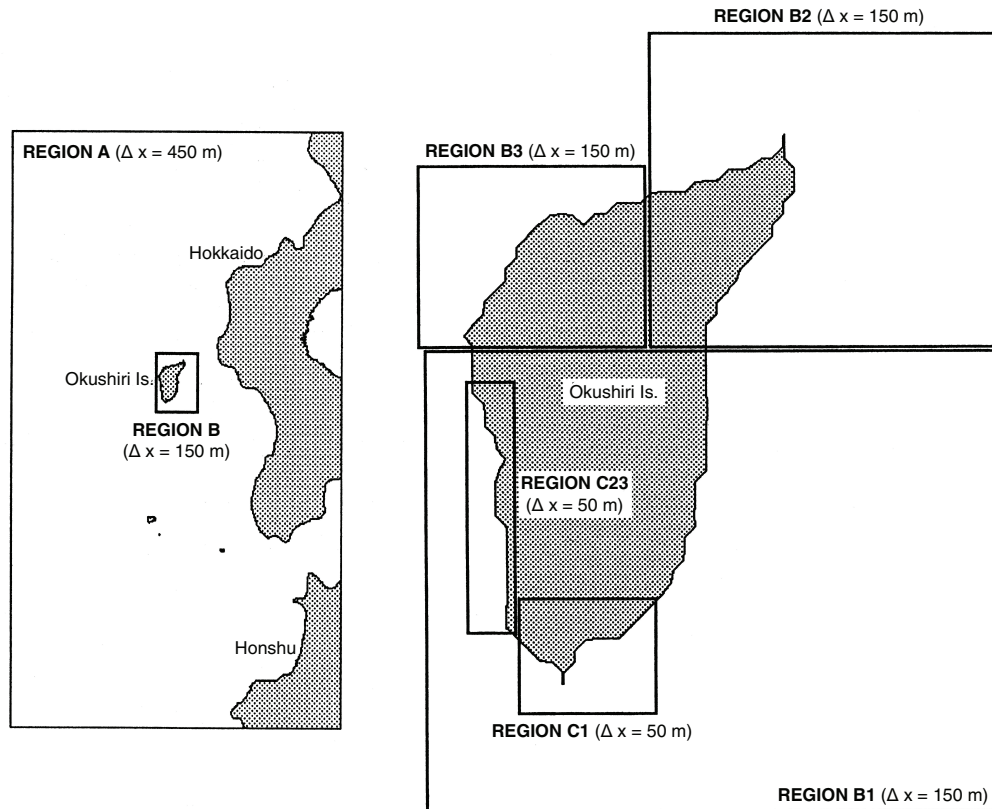
**Figure A33:** Bathymetric data provided by the Disaster Control Research Center, Japan.

Hamatsumae, located to the east of Aonae, needs to be explained since Hamatsumae is sheltered against the direct attack of the tsunami by the Aonae point. Also, topography does not suggest any tsunami amplification mechanism at this location.

- The highest runup of 31.7 m in a valley north of Monai needs to be approximated with the numerical model (Fig. A37).
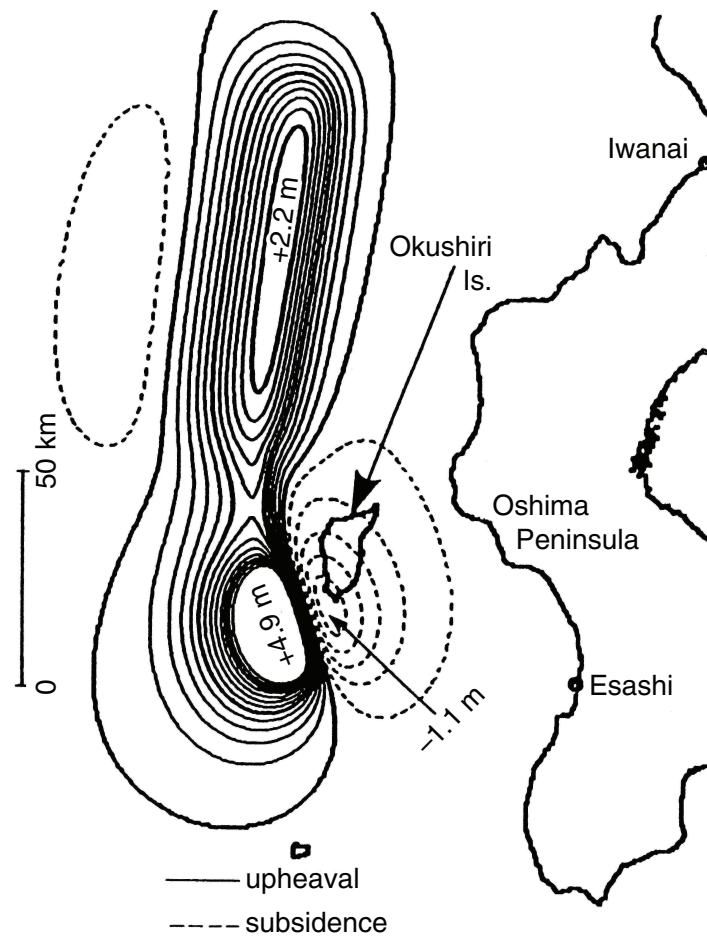
**Figure A34:** Fault plane DCRC-17a constructed by the Disaster Control Research Center, Japan.
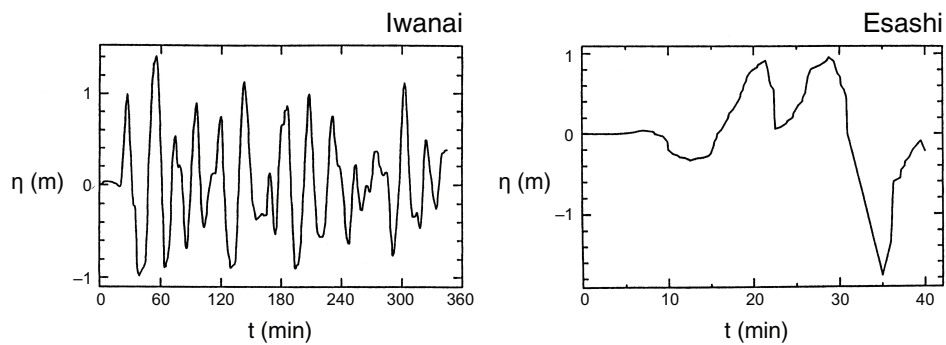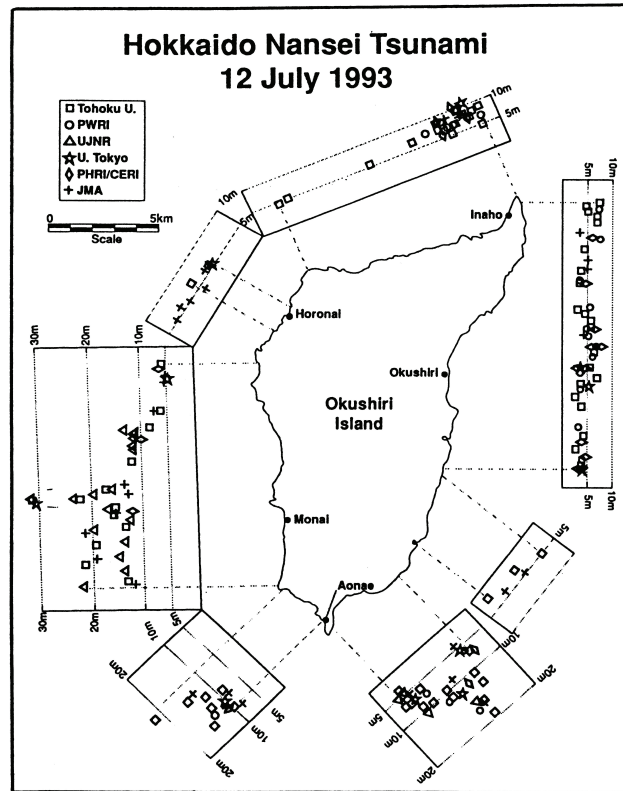


**Figure A35:** Tide gage data at Iwanai and Esashi.

**Figure A36:** Maximum runup measurements around Okushiri Island.
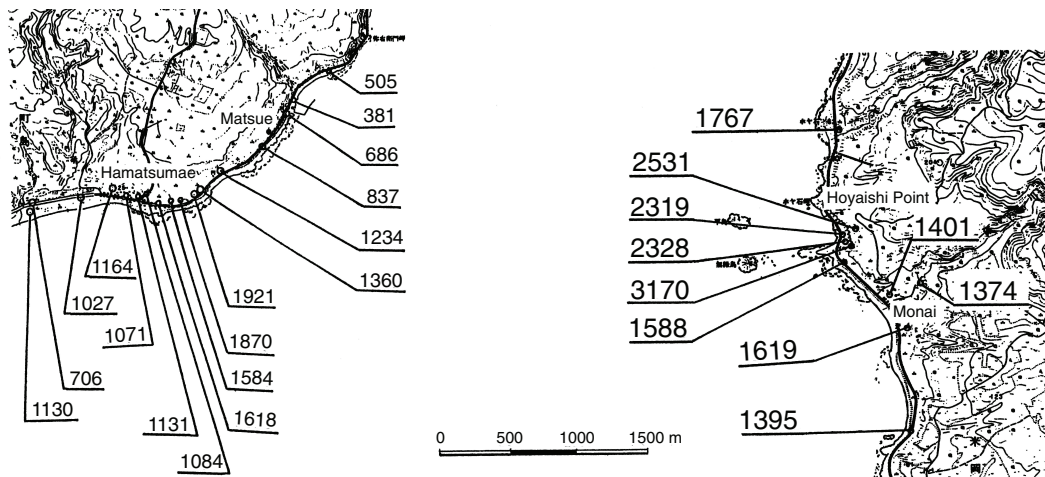


**Figure A37:** Detailed runup distribution at Hamatsume and north of Monai.

### 4.2   Rat Islands tsunami

Observation data from the expanding tsunami observation network will continue to provide more data for model verification. NOAA's National Geophysical Data Center (`http://www.ngdc.noaa.gov/seg/hazard/tsu.shtml`), NOAA's Tsunami Warning Centers (`http://wcatwc.arh.noaa.gov/`), and NOAA's Center for Tsunami Research websites provide updated information on the latest tsunami data. Here, we present the data used for the first real-time model forecast test as an example of data use for model verification.

The magnitude $M_w = 7.8$ earthquake was located on the shelf near Rat Islands, Alaska, on 17 November 2003 and generated a tsunami. This tsunami provided good data for testing operational models, since the tsunami was detected by three tsunameters located along the Aleutian Trench and was recorded at many coastal locations (Titov *et al.*, 2005). This was the first real-time tsunami detection by the newly developed tsunameter system (DART). In addition, for the first time, tsunami model predictions were obtained during the tsunami propagation, before the waves had reached many coastlines. Here, the combined use of tsunami propagation and inundation models is required for simulation of tsunami dynamics from generation to inundation. The test requires matching the propagation model data with the DART recording to constrain the tsunami source model (Fig. A38). If a finite-difference method on a structured grid is used, several nested numerical grids would allow "telescoping" from a coarse-resolution propagation model into a high-resolution inundation model with a model grid of at least 50 m resolution. If an unstructured grid method is used, a single grid may include enough resolution near the coast. The data-constrained propagation model should drive the high-resolution inundation model of Hilo Harbor. The inundation model is to reproduce the tide gage record at Hilo (Fig. A39). Since this benchmarking is required for the forecasting models, it is essential to model 4 hr of Hilo Harbor tsunami dynamics in 10 min of computational time.
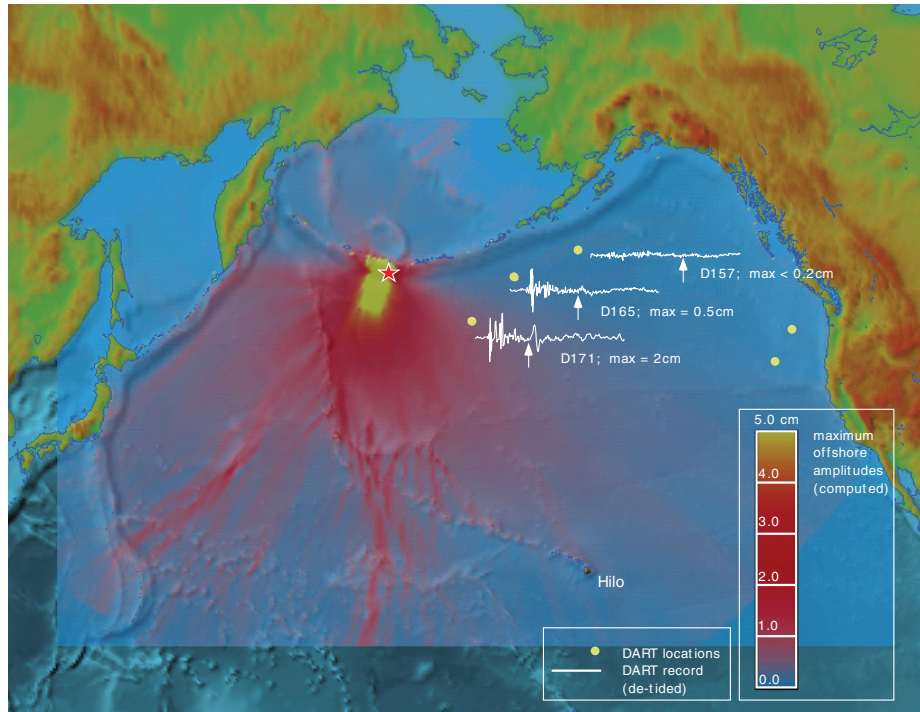
**Figure A38:** Propagation of the 17 November 2003 Rat Islands tsunami. Star indicates epicenter location of the earthquake. Yellow dots are locations of DART systems. White lines near the DART locations show recorded tsunami signal (detided) at corresponding tsunameter, arrows indicate tsunami arrival on the recordings. Filled colors show example of computed maximum tsunami amplitudes of a model propagation scenario.
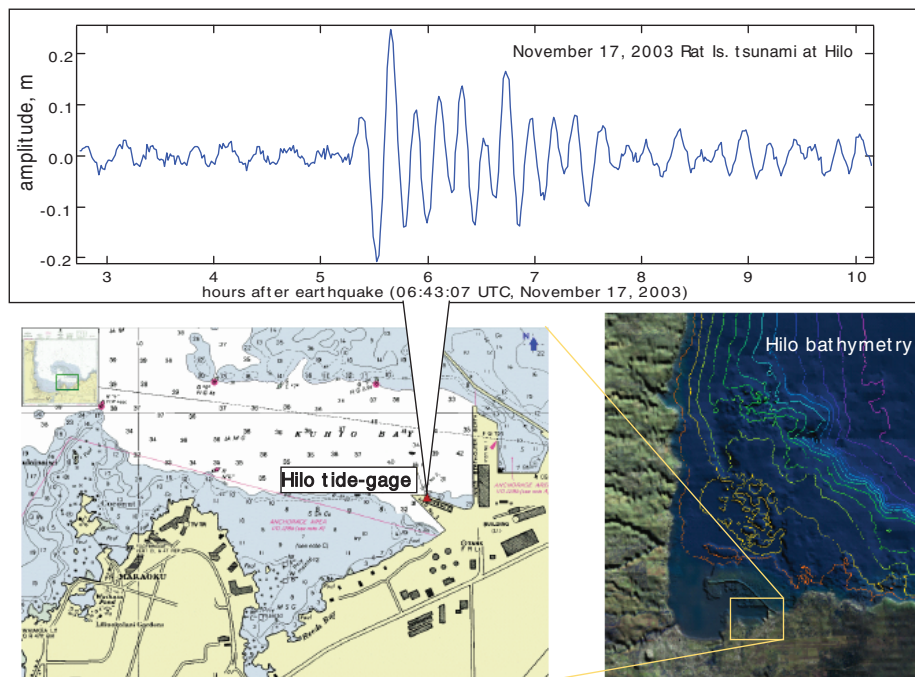


**Figure A39:** Location of Hilo tide gage and the recording of the 17 November 2003 Rat Islands tsunami.